M. Klug et al.

Supplementary Information for *Metal composition influences optoelectronic quality in mixed-metal lead-tin triiodide perovskite solar absorbers*

Matthew T. Klug[1], Rebecca L. Milot[1,2], Jay B. Patel[1], Thomas Green[1], Harry C. Sansom[1], Michael D. Farrar[1], Alexandra J. Ramadan[1], Samuele Martani[3], Zhiping Wang[1], Bernard Wenger[1], James M. Ball[1], Liam Langshaw[1], Annamaria Petrozza[3], Michael B. Johnston[1], Laura M. Herz[1], Henry J. Snaith[1,*]

[1]Department of Physics, University of Oxford, Clarendon Laboratory, Parks Road, Oxford OX1 3PU, United Kingdom

[2]Department of Physics, University of Warwick, Gibbet Hill Road, Coventry CV4 7AL, United Kingdom

[3]Center for Nano Science and Technology @Polimi, Istituto Italiano di Tecnologia, Milan, Italy

*email: henry.snaith@physics.ox.ac.uk

Experimental Methods

Materials. Lead (II) iodide (ultra dry 99.999%, PbI_2), tin (II) iodide (ultra dry 99.999%, SnI_2), cesium iodide (99.9%, CsI), and bathocuproin (98%, BCP) were sourced from Alfa Aesar. Tin (II) fluoride (99%, SnF2), lead (II) thiocyanate (99.5%, $Pb(SCN)_2$), poly(methyl methacrylate) (PMMA), acetic acid (≥99.99%), chlorobenzene (anhydrous 99.8%, CB), 1,2-dichlorobenzene (anhydrous 99%, DCB), *N,N*-dimethylformamide (anhydrous 99.8%, DMF), dimethyl sulfoxide (anhydrous ≥99.9%, DMSO), 2-propanol (anhydrous 99.5%, IPA) and toluene (anhydrous 99.8%) were sourced from Sigma-Aldrich. Poly[bis(4-phenyl)(2,4,6-trimethylphenyl)amine] (PTAA) was sourced from Flexink. Poly [(9,9-bis(3'-(N,N-dimethylamino)propyl)-2,7-fluorene)-alt-2,7-(9,9–dioctylfluorene)] (PFN-P1) was sourced from 1-Material. Phenyl-C61-butyric acid methyl ester (99.5%, PCBM) was sourced from Solenne BV. Silver shot (99.99% 1-3 mm granules, Ag) was sourced from Testbourne Ltd. Formamidinium iodide (FAI) was sourced from GreatCell Solar. Fluorine-doped tin oxide (TEC15, FTO) coated glass was sourced from Hartford Glass. Indium tin oxide (ITO) coated glass were sourced from Shezhen Huyu Union Technology. Methanol was sourced from Fisher Scientific. Poly(3,4-ethylenedioxythiophene)-poly(styrenesulfonate) (P VP AI 4083, PEDOT:PSS) was sourced from Heraeus.

PFN Solution Preparation. A solution of 0.1 mg/mL PFN was prepared by using methanol to dilute a stock solution of 0.5 mg/mL in methanol with 2 µL/mL of glacial acetic acid. The 0.1 mg/mL PFN solution was filtered before use with a 2 µm glass microfiber filter.

Perovskite Solution Preparation. A stock solution of 1.2M $(FA_{0.83}Cs_{0.17})PbI_3$ solution (*i.e.* 0% Sn) with 6% molar excess $Pb(SCN)_2$ was prepared by dissolving 856.4 FAI, 265.0 CsI, 2,766.1 mg PbI_2, and 116.4 mg $Pb(SCN)_2$ in 5 mL of a mixed solvent of 4:1 DMF:DMSO by volume (*i.e.* 4 mL DMF and 1 mL DMSO). A stock solution of 1.2M $(FA_{0.83}Cs_{0.17})(Pb_{0.3}Sn_{0.7})I_3$ (*i.e.* 70% Sn) with 6% molar excess of $Pb(SCN)_2$ with respect to the PbI_2 content and 10% molar excess of SnF_2 with respect to the SnI_2 content was prepared by dissolving 856.4 mg FAI, 265.0 mg CsI, 829.8 mg PbI_2, 1,564.6 mg SnI_2, 65.8 mg SnF_2, and 34.9 mg $Pb(SCN)_2$ in 5 mL of a mixed solvent of 4:1 DMF:DMSO by volume. Solutions with Sn content = {10, 20, 30, 40, 50, 60}% were prepared by mixing the 0% and 70% Sn stock solutions in the appropriate ratio. Solutions with Sn content = {0.001, 0.01, 0.1, 0.5, 1, 5}% were prepared through serial dilution of the 10% Sn solution with the 0% Sn solution. The solutions were left to age for 10 days without stirring. Prior to spin-coating, the supernatant of the perovskite solution was filtered with a 0.45 µm PTFE syringe filter.

Solar Cell Fabrication. The TEC15 FTO substrates were prepared by patterning the electrode via etching with zinc powder and an aqueous 2M HCl solution. They were then cleaned through a sequential

process of sonication in a soap solution (diluted Hellamanex in water), rinsing with deionized water, acetone, and isopropanol. The residual solvent was dried off the substrate by a stream of compressed air. Immediately prior to spin-coating the device layers, the cleaned substrates were subjected to a UV-ozone treatment for 20 minutes. The substrates were then transferred into a nitrogen glove box for the remainder of device processing.

A PTAA layer (~15 nm) was prepared on the UV-ozone treated FTO substrates by statically dispensing 200 µL of a filtered (200 nm PTFE) solution (1 mg/mL PTAA in toluene) at 4 krpm for 30 s with a 4 s ramp, followed by annealing at 130°C for 10 minutes. Once cooled to room temperature a layer of PFN was deposited by statically dispensing 200 µL of the PFN solution (0.1 mg/mL) and spin-coating at 5 krpm for 20 s with 5 s ramp. The PFN layer was not annealed following spin-coating.

The perovskite layer was prepared by statically dispensing 100 µL on the FTO/PTAA/PFN substrates and spin-coating at 4.5 krpm for 14s with a 6s ramp. 25s after the spin-coating began, 300 µL of anisole was dropped onto the spinning substrate. Immediately after the spin-coating program finished, a stream of N_2 gas was applied to the substrate for 15s, during which the film continued to darken. Afterwards, the substrate was annealed at 120°C for 30 minutes.

A PCBM layer (~20 nm) was deposited by dynamically dispensing 50 µL of a warm solution (20 mg/mL PCBM in 3:1 CB:DCB by volume, 90°C) onto pre-warmed perovskite substrates (90°C) and spin-coating at 2 krpm for 30s. The PCBM layers were annealed at 90°C for 5 minutes. Once cooled to room temperature, a layer of BCP was deposited by dynamically dispensing 70 µL of solution (0.5 mg/mL BCP in IPA) and spin-coating at 4 krpm for 20 s without any post-anneal.

A 150 nm thick Ag top electrode was thermally evaporated onto the device.

Optimal 1.33 eV Solar Cell Fabrication. Patterned ITO substrates were cleaned through sequential sonication in acetone and isopropanol. The residual solvent was dried off the substrates by flowing a stream of compressed air. Immediately prior to spin-coating the device layers, the substrates were cleaned with an oxygen plasma for 15 minutes and then transferred into a nitrogen glove box for the remainder of device processing.

A PTAA layer was prepared on the plasma-treated ITO substrates by statically dispensing 200 µL of a filtered (200 nm PTFE) solution (0.3 mg/mL PTAA in toluene) at 4 krpm for 30 s with a 4 s ramp, followed by annealing at 130°C for 10 minutes. Once cooled to room temperature a layer of PFN was deposited by statically dispensing 200 µL of the PFN solution (0.1 mg/mL) and spin-coating at 5 krpm for 20 s with 5 s ramp. The PFN layer was not annealed following spin-coating.

The perovskite solution was prepared the same as described above, except that 5% $Pb(SCN)_2$ molar excess over the PbI_2 content was used instead of 6%. The perovskite layer was prepared by statically dispensing 100 µL on the ITO/PTAA/PFN substrates and spin-coating at 5 krpm for 14s with a 6s ramp. 13s after the spin-coating began, 300 µL of anisole was dropped onto the spinning substrate. Immediately after the spin-coating program finished, a stream of N_2 gas was applied to the substrate for 15s, during which the film continued to darken. Afterwards, the substrate was annealed at 120°C for 15 minutes. The deposition of the PCBM n-type contact layer, the BCP interlayer, and the Ag top electrodes were performed with the same procedure described above for the solar cells prepared on FTO.

Optimal 1.30 eV Solar Cell Fabrication. Patterned ITO substrates were cleaned through sequential sonication in acetone and isopropanol. The residual solvent was dried off the substrates by flowing a

stream of compressed air. Immediately prior to spin-coating the device layers, the substrates were cleaned with an oxygen plasma for 15 minutes. A PEDOT:PSS layers was prepared by statically dispensing 180 µL of a filtered (0.45 µm glass microfibre) solution (1:2 ratio of (PEDOT:PSS):methanol by volume) was statically spin-coated at 4 krpm for 40s with a 1s ramp and then annealed at 150°C for at least 10 minutes. The substrates were then transferred into a nitrogen glove box and annealed again at 120°C for 10 minutes.

The perovskite solution was prepared the same as described above, except that 20% SnF_2 molar excess over the SnI_2 content was used instead of 10%. The perovskite layer was prepared by statically dispensing 110 µL on the ITO/PEDOT:PSS substrates and spin-coating at 3.6 krpm for 14s with a 6s ramp. 13s after the spin-coating began, 300 µL of anisole was dropped onto the spinning substrate. Immediately after the spin-coating program finished, a stream of N_2 gas was applied to the substrate for 15s, during which the film continued to darken. Afterwards, the substrate was annealed at 120°C for 10 minutes. The deposition of the PCBM n-type contact layer, the BCP interlayer, and the Ag top electrodes were performed with the same procedure described above for the solar cells prepared on FTO.

Optical-Pump/Terahertz Probe (OPTP) Sample Preparation. Perovskite films were deposited on O_2-plasma treated quartz discs using the same method as the devices. Quartz was used as a substrate owing to it low absorption coefficient at terahertz frequencies.[1]

Photoluminescence Sample Preparation. Perovskite films were deposited onto O_2-plasma treated glass substrates using the same method as the devices. Samples that were measured in ambient environment were encapsulated with a glass coverslip and sealed using a UV-curable resin.

Conductivity Sample Preparation. Perovskite films were deposited on an O_2-plasma treated glass substrate using the same method as the devices. A 75 nm thick gold electrode pattern of a standard four-point probe conductivity design with a 0.5 mm probe spacing was thermally evaporated directly onto the bare perovskite films.

Photothermal Deflection Spectroscopy Sample Preparation. Perovskite films were deposited on an O_2-plasma treated quartz substrate using the same method as the devices.

Scanning Electron Microscopy, Absorbance, and X-ray Diffraction Sample Preparation. The glass backside of TEC15 substrates were pre-scribed into quarters using a diamond scribe. The samples were prepared identically to the devices (i.e. UV-ozone treatment, PTAA deposition, PFN deposition, and perovskite deposition). After the perovskite film was prepared, the substrate was snapped into quarters. One quarter was used for imaging with SEM. An XRD samples was prepared by depositing a capping layer of PMMA on another quarter by dynamically spin-coating 50 µL a PMMA solution (10 mg/mL in CB) at 2 krpm for 30s. The PMMA layer was deposited to keep moisture off of the substrates during x-ray diffractometry measurements. A third quarter was used for UV-Vis-NIR absorbance measurements.

Characterisation Methods

Photovoltaic Characterisation of Solar Cells. Current-voltage (JV) characteristics of the solar cells were recorded in ambient air under simulated AM1.5 solar light (1-Sun, 100 mW cm^{-2}) generated by an ABET Class AAB sun 2000 simulator. The solar simulator was calibrated for two different perovskite bandgaps: 1.6 eV and 1.2 eV. The 1.6 eV calibration was performed using a certified KG3 filtered silicon reference cell and the 1.2 eV calibration was performed using a certified KG2 filtered silicon

reference cell. Each device was measured with a 20 mV voltage step and a 100 ms time step (*i.e.* scan rate of 0.2 V/s) using a Keithley 2400 source meter. All devices were masked with a 0.0919 cm^2 metal aperture to define the active area and eliminate edge effects. Steady-state power output (SPO) measurements were performed by holding the device at the voltage of the maximum power point, as determined by the JV characteristic, and monitoring the current density over the course of 60 s.

External Quantum Efficiency (EQE) Characterisation of Solar Cells. The external quantum efficiency (EQE) was measured using a homemade setup comprised of a 250 W halogen lamp, a monochromator (Princeton Instruments SP2150), an optical chopper (Thorlabs), and a lock-in amplifier (Stanford Research SR830). The system was calibrated with a NIST-traceable calibrated Si photodiode (Thorlabs FDS100-CAL) immediately before measuring the perovskite samples. EQE measurements were made immediately after JV and SPO measurements.

Fourier-Transform Photocurrent Spectroscopy (FTPS). The EQE to calculate the Urbach energy was measured via a custom-built Fourier transform photocurrent spectrometer based on a Bruker Vertex 80v Fourier Transform Interferometer coupled with a Stanford Research 570 current preamplifier. Devices were illuminated with a class AAA, oriel solar simulator. The solar cells were masked with a metal aperture, with a defined active area, 0.0625 cm^2.

A non-linear regression was performed using MATLAB to extract the Urbach energy from the EQE data. Robust fitting was performed using a bisquared (Tukey's biweight) weighting function. We calculated a 95% confidence interval for the Urbach energy using the residuals and Jacobian of the fit.

Electroluminescence Characterisation of Solar Cells. Solar cells were loaded into a hermetically sealed chamber testing chamber loaded with a nitrogen atmosphere, which is attached to the port of an integrating sphere. Voltage is supplied to the desired pixel using a Keithley 2400 source meter and the emitted light is collected with a Maya Pro Spectrophotometer (Ocean Optics).

X-ray Diffraction (XRD). Powder X-ray diffraction patterns were obtained using a Panalytical X'pert powder diffractometer (Cu-Kα1 radiation; λ = 154.05 pm) at room temperature with a Bragg-Brentano geometry. During measurement, rotation of the sample was enabled to improve the detection statistics.

Film Thicknesses. The film thicknesses were measured using a Veeco Dektak profilometer to determine, which were used for the conductivity measurement analysis.

Four-Point Probe Conductivity. Conductivity measurements were made using a homemade four-point probe setup, with a force channel length (direction of current flow) of 1.5 mm and a width of 5.5 mm and a sense channel length of 500 μm and width of 750 μm. The current-voltage characteristics of these samples were collected at room temperature with a Keithley 2420 source meter unit to extract both the bulk and the contact resistance. The contact resistance was found to be negligible compared to the bulk. First, measurements under dark conditions were measured with the samples under aluminium foil. Light measurements were then taken using an LED lamp with an equivalent illumination of approximately 0.1 sun.

Photoluminescence Spectra. The time-averaged photoluminescence (PL) spectra were obtained following excitation at 400 nm from a frequency-doubled pulsed laser source (Mai-Tai-Empower-Spitfire from Spectra Physics, 35 fs pulse duration, 5 kHz repetition rate, 800 nm center wavelength). The scattered PL was collected by a lens placed ~130 mm from the sample, and an optical fiber directed the light toward an imaging spectrometer (Horiba, iHR320). The light was then detected using a nitrogen-cooled CCD or InGaAs array as appropriate for the emission wavelength. All measurements

were performed in vacuum, and spectra were recorded for each sample at several irradiances ranging from $1.5 – 75$ µJ/cm^2. As no changings in spectral features were observed with changes in irradiance, only spectra obtained at the highest irradiances are reported in Figure S2.

UV-Vis-NIR Spectrophotometry. Optical absorbance measurements of encapsulated perovskite thin-films were made using a long-range PerkinElmer Lambda 1050 UV/VIS/NIR spectrometer scanning between 600-1100 nm at 2 nm increments.

Time-Resolved Photoluminescence. Time-resolved PL measurements were made on encapsulated films using a PicoQuant FluoTime 300 time-correlated single-photon counter (TCSPC) instrument using a 507 nm laser diode as the illumination source.

Photoluminescence Quantum Efficiency (PLQE). PLQE measurements were made using the procedure previously reported by de Mello et al.[2] In brief, encapsulated PL samples were placed in an integrating sphere equipped with a Maya Pro spectrophotometer (Ocean Optics) and illuminated with a 532 nm laser diode. The emission spectrum was measured under four separate conditions: (1) when the sample is loaded by the laser is off, (2) when the sample is not loaded but the laser is on, (3) when the sample is loaded and illuminated with the laser, and (4) when the sample is loaded and the laser is on, but the sample is not illuminated. This procedure was repeated for several different laser intensities, where the laser was filtered through neutral density filters with different optical densities. The laser power for each intensity was measured using a thermopile detector (Gentec-EO) and the beam size was determined using the knife-edge technique.

Optical-Pump/Terahertz-Probe (OPTP). OPTP measurements were performed using an amplified laser system (Mai-Tai-Empower-Spitfire from Spectra Physics) with 5 kHz repetition rate, 35 fs pulse duration, and 800 nm center wavelength. The output of the laser was split into three beams: one for generating THz radiation to probe the sample, another for detecting THz radiation, and a third for optically pumping the sample. THz radiation was generated in a metallic spintronic emitter via the inverse spin hall effect[3,4] and detected using free-space electro-optic sampling in 0.2 mm thick GaP(110) crystal and a pair of balanced photodiodes. The samples were photoexcited at 400 nm following frequency doubling of the fundamental laser output in a BBO crystal, and the change in amplitude of the peak of the THz pulse ($\Delta T/T$) was monitored as a function of the pump-probe delay time. Data obtained following excitation at fluences of 4-5 µJ/cm^2 were used for the calculation of charge-carrier mobility as described below. All measurements were performed in vacuum.

Scanning Electron Microscopy (SEM). Film morphology imaging was performed with a Hitachi S-3400 SEM operating with a 3 kV accelerating voltage and a 10 µA probe current.

Microstrain Analysis. The lattice microstrain was estimated by applying a modified Williamson-Hall approach to the powder X-ray diffraction patterns, as was presented in McMeekin et al.[5]

Photothermal Deflection Spectroscopy (PDS). Each sample was placed in a cuvette filled with a transparent fluid (tetradecafluorohexane) whose refractive index has a considerable temperature dependence. When the sample absorbs a monochromatic excitation light, it releases the heat into the portion of the fluid that surrounds its surface, generating a thermal lens (mirage effect). By measuring the deflection of a laser beam (HeNe) aligned parallel and in close proximity to the sample's surface, the fluid refractive index change caused by the heat generation can be accurately quantified. The measured deflection is linearly proportional to the absorbance of the sample (considering small deflection angles) and by varying the excitation wavelength the sub-bandgap absorption spectrum can

be retrieved. The excitation is provided by a supercontinuum white laser filtered by a monochromator and modulated by an optical chopper (lock-in detection). The laser provides a higher power and better focusing than high power lamps.

The laser emission spectrum was measured using two photodiodes (one for the visible, the other for the near infrared) to normalise the deflection signal. The figure was obtained combining absolute absorbance data from a spectrophotometer (UV-Vis) and several PDS measurements performed in different parts of the spectrum. Long pass filters were added to reject unwanted leaked light from the monochromator.

X-ray Photoelectron Spectroscopy (XPS). X-ray photoemission spectroscopy measurements were carried out using a Thermo Scientific Kα X-ray spectrometer. An Al Kα X-ray source was used at a take-off angle of 90°. Valence band (VB) and survey spectra were measured using a pass energy of 20 eV and 50 eV respectively, from an analysis area of 400 μm x 400 μm. The spectrometer work function and binding energy scale were calibrated using the Fermi edge and 3d peak recorded from a polycrystalline Ag sample prior to the commencement of the experiments. VB-XPS exploits the high photon energies of the X-ray light source (1487 eV for Al Kα) to measure the density of states of the valence band of a sample with a reduction in surface specificity (compared with ultraviolet photoemission spectroscopy, typically several atomic layers) and therefore such measurements are often considered to be more characteristic of the properties of the bulk sample.[6,7] We note that we are unable to quantify the exact position of the Fermi level in these samples since the instrument was unable to apply the bias necessary to account for the work function of the instrument itself as well as charging. Therefore, we are unable to quantify the energy difference between the valence band and Fermi level but are able to examine trends across the specimen series since the offset is likely to be constant, and a function of the instrument rather than the films themselves.

Scanning Electron Microscopy
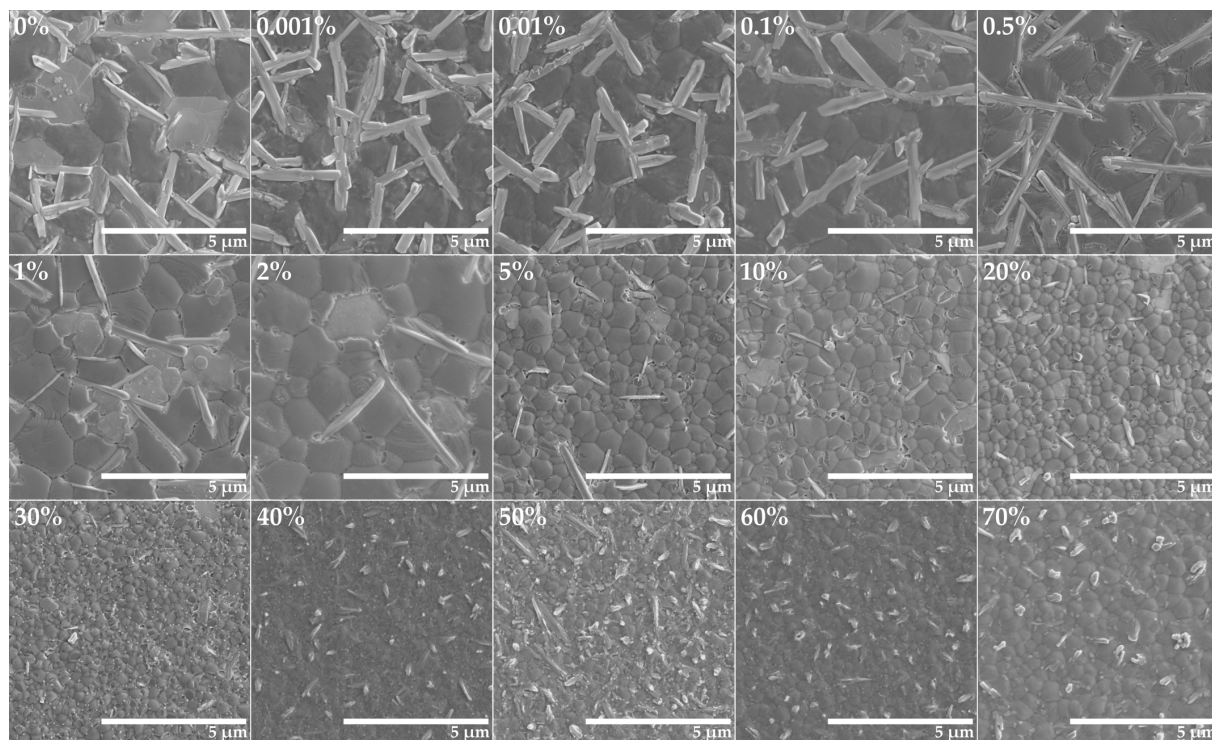
Figure S1. Scanning electron micrographs of $(FA_{0.83}Cs_{0.17})(Pb_{1-y}Sn_y)I_3$ with a 10% excess of SnF_2 with respect to the SnI_2 content and a 6% excess of $Pb(SCN)_2$ with respect to the PbI_2 content. The percentage of the metal iodide content that is Sn is written in the upper left corner of each panel.

Absorbance and Steady State Photoluminescence Spectroscopy
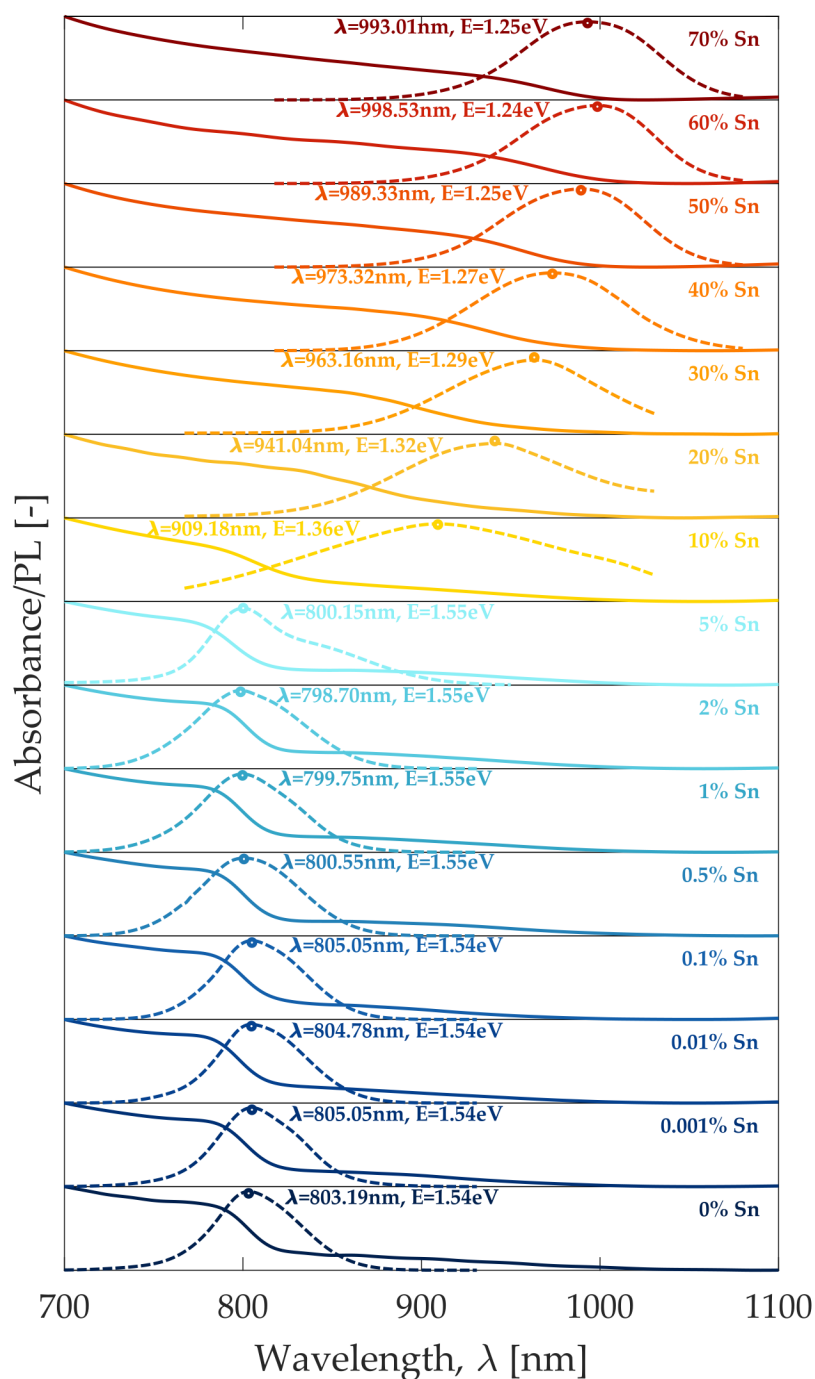
Figure S2. UV-Vis-NIR absorbance (solid lines) and steady-state photoluminescence spectra (dotted lines) of $(FA_{0.83}Cs_{0.17})(Pb_{1-y}Sn_y)I_3$ with a 10% excess of SnF_2 with respect to the SnI_2 content and a 6% excess of $Pb(SCN)_2$ with respect to the PbI_2 content. The PL peak is denoted with an open circle and the peak position is annotated for each composition.
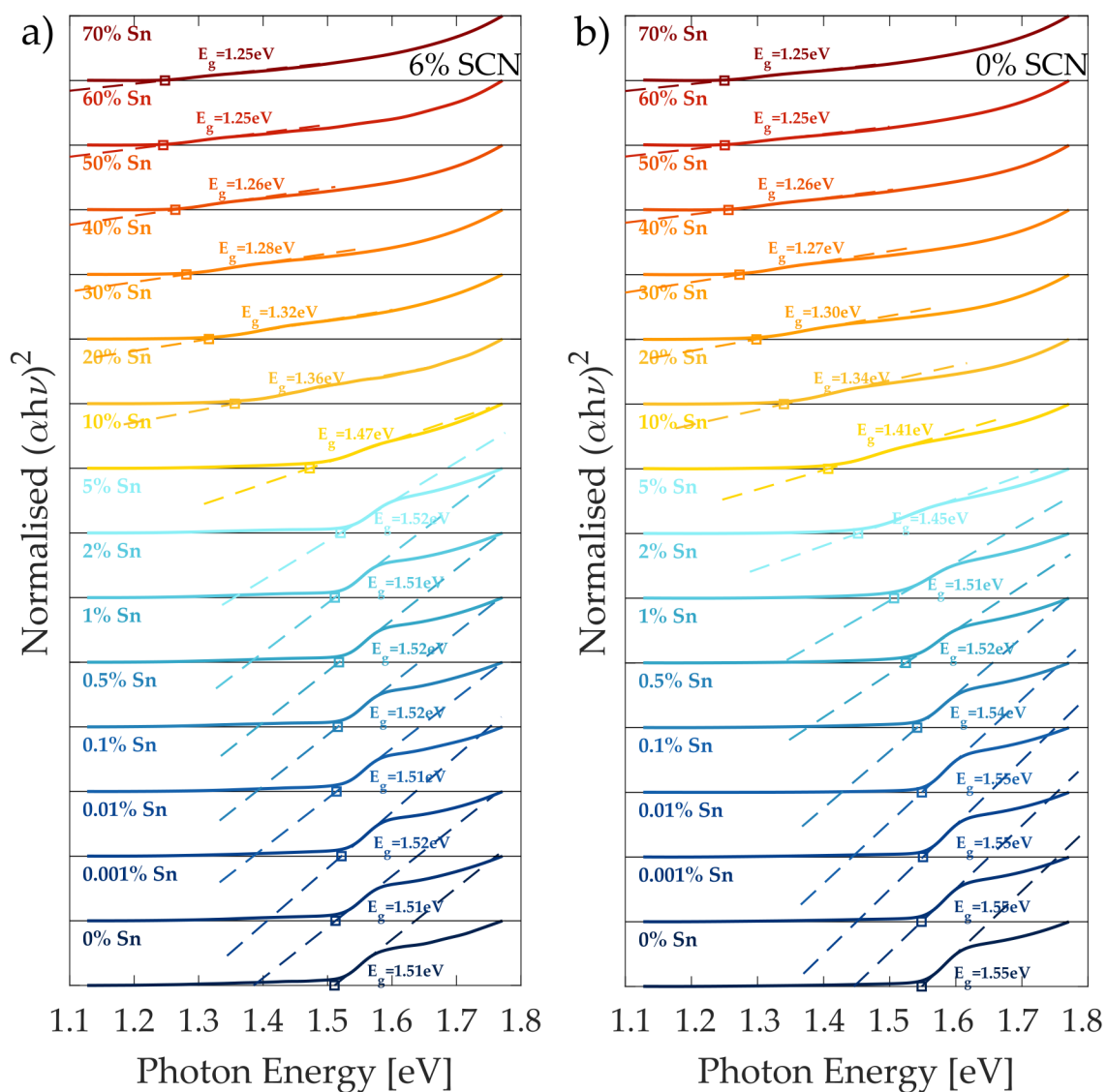
Figure S3. Tauc plots determined from UV-Vis-NIR absorption spectra for $(FA_{0.83}Cs_{0.17})(Pb_{1-y}Sn_y)I_3$ compositions prepared with (a) 6% and (b) $Pb(SCN)_2$ with respect to PbI_2.

External Quantum Efficiency Derivative
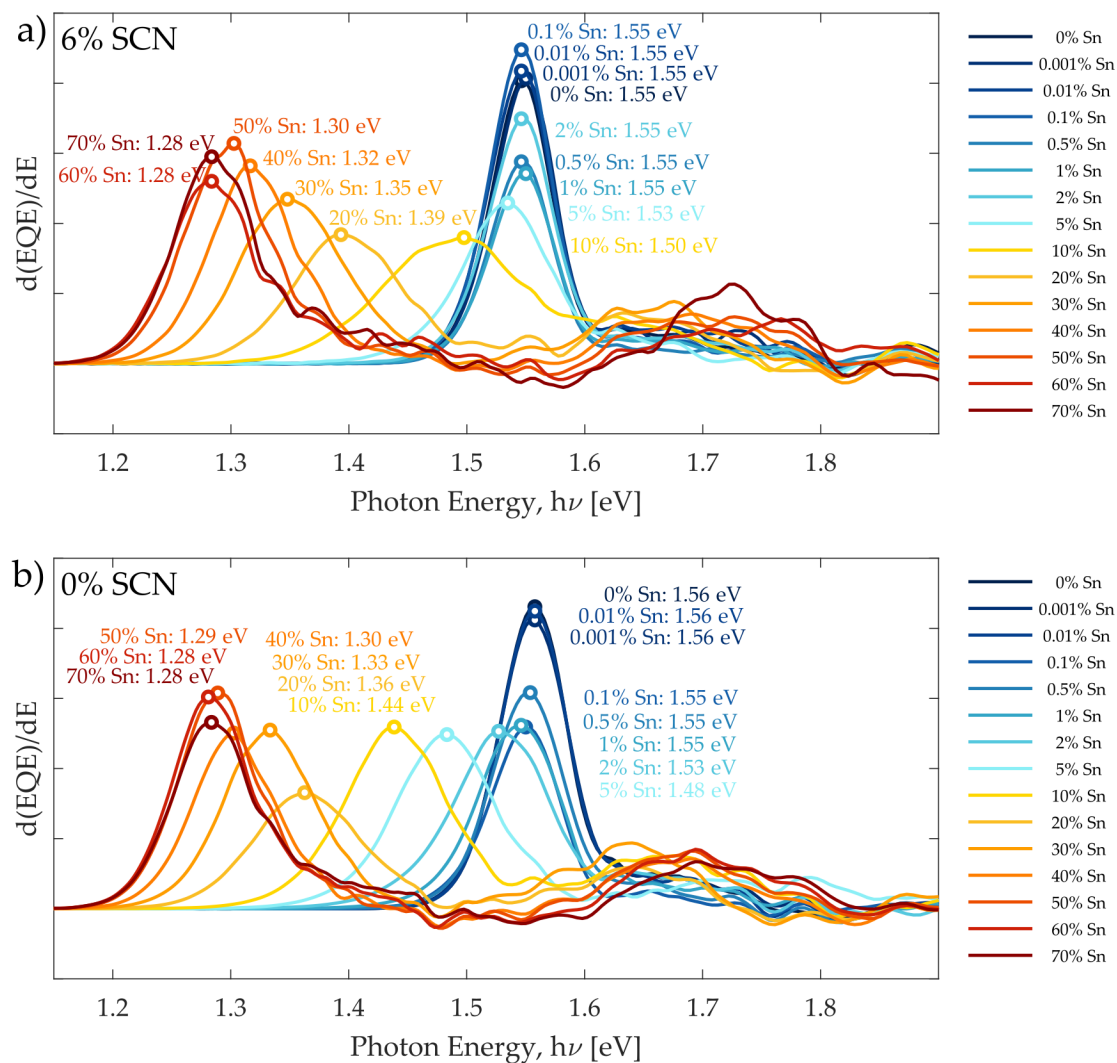
Figure S4. Derivative of EQE with respect to photon energy for $(FA_{0.83}Cs_{0.17})(Pb_{1-y}Sn_y)I_3$ compositions prepared with either (a) 6% and (b) 0% $Pb(SCN)_2$ with respect to PbI_2. Circle marker indicates the peak position, for which the value is printed.

Energy &
Environmental Science

Powder X-ray Diffraction
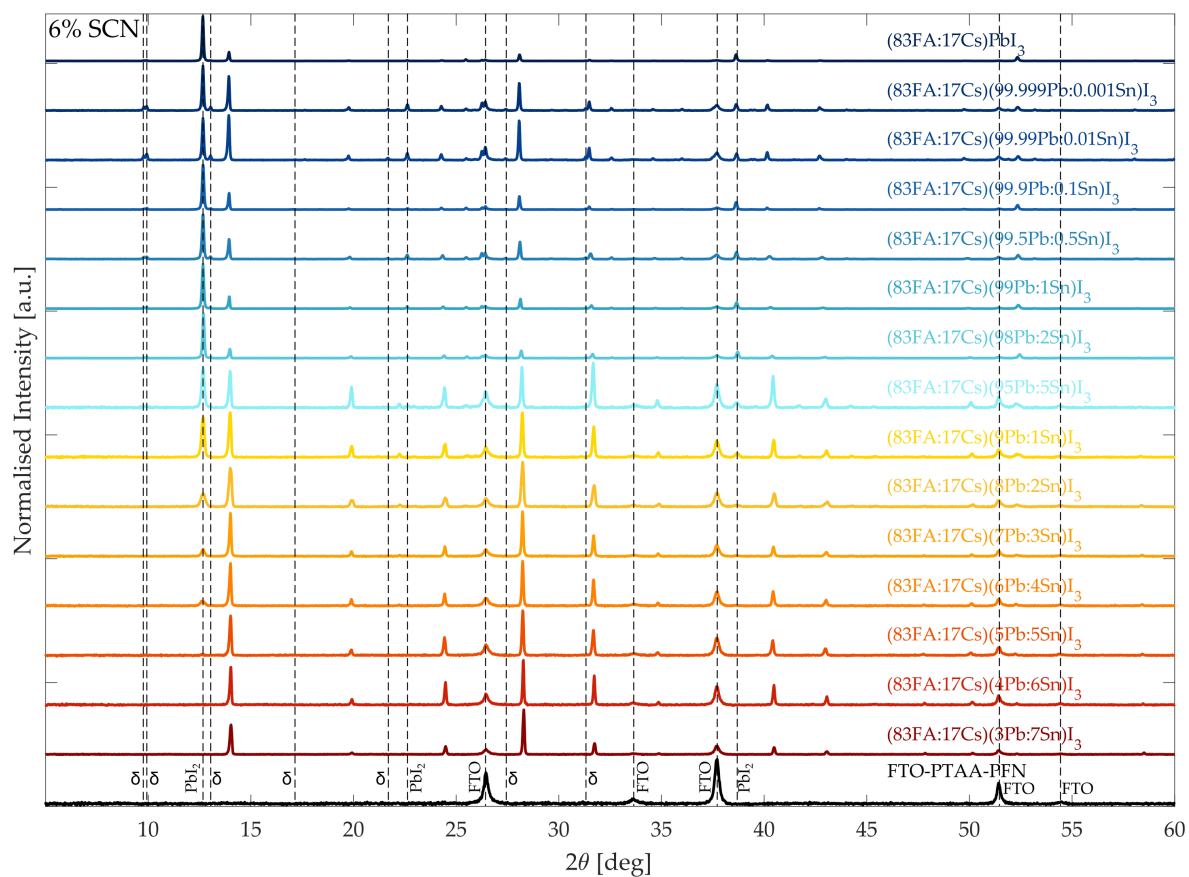
Figure S5. Powder X-ray diffractograms of $(FA_{0.83}Cs_{0.17})(Pb:Sn)I_3$ thin-films prepared on a FTO/PTAA/PFN stack. All films have are prepared with a 10% excess of SnF_2 with respect to the SnI_2 content and a 6% excess of $Pb(SCN)_2$ with respect to the PbI_2 content. Impurity phases of PbI_2 and δ-$CsPbI_3$ (denoted with δ) are indicated.

External Quantum Efficiency

a)

b)
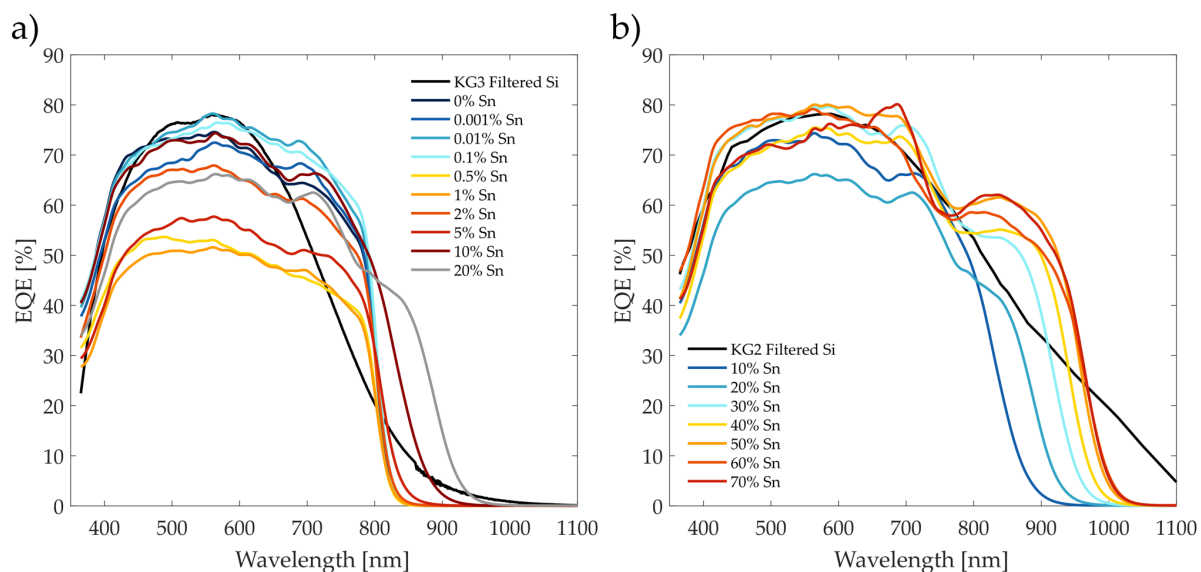
Figure S6. Representative external quantum efficiency spectra for $(FA_{0.83}Cs_{0.17})(Pb_{1-y}Sn_y)I_3$ devices with (a) low and (b) high Sn content. The perovskite films have been prepared with a 10% excess of SnF_2 with respect to the SnI_2 content and a 6% excess of $Pb(SCN)_2$ with respect to the PbI_2 content. The filtered silicon reference cell used for the solar sim calibration and mismatch calculations is indicated in each by a black line.

a)

b)
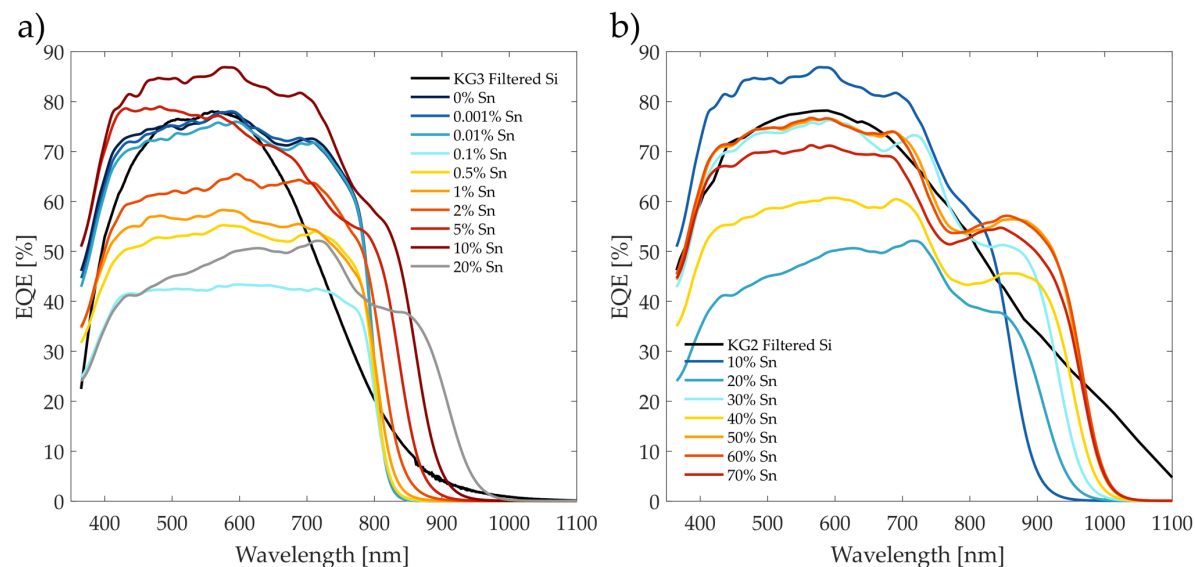
Figure S7. Representative external quantum efficiency spectra for $(FA_{0.83}Cs_{0.17})(Pb_{1-y}Sn_y)I_3$ devices with (a) low and (b) high Sn content. The perovskite films have been prepared with a 10% excess of SnF_2 with respect to the SnI_2 content and no $Pb(SCN)_2$. The filtered silicon reference cell used for the solar sim calibration and mismatch calculations is indicated in each by a black line.

Spectral Mismatch Calculation
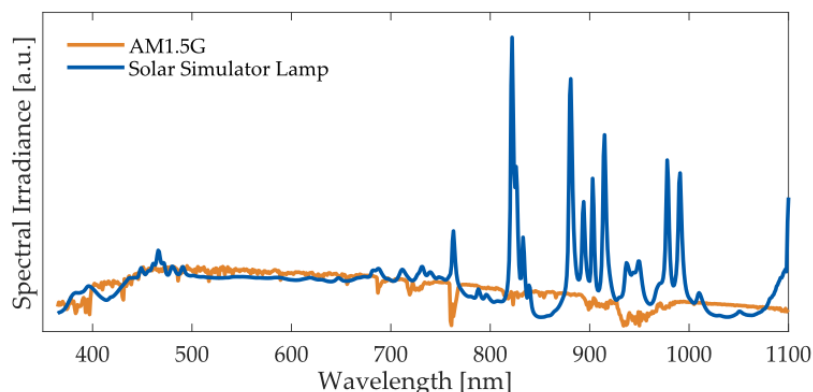
Figure S8. Spectral irradiance of the solar simulator lamp and the AM1.5G standard solar spectrum.
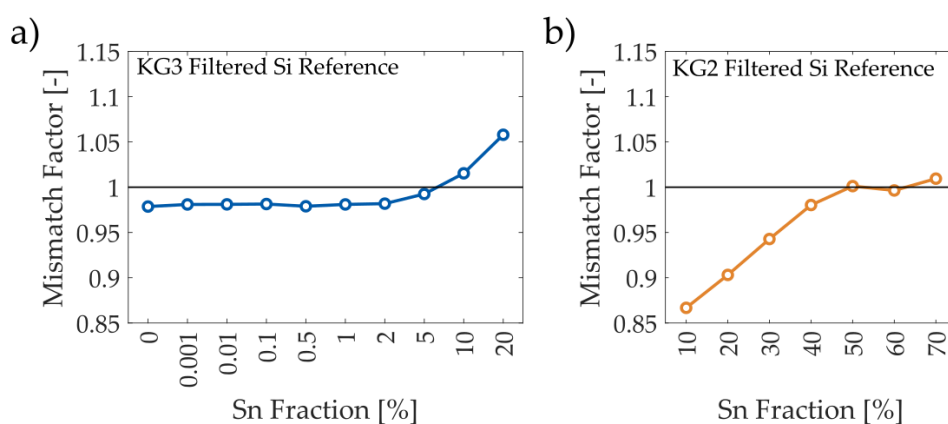
Figure S9 Spectral mismatch factor calculated for $(FA_{0.83}Cs_{0.17})(Pb_{1-y}Sn_y)I_3$ compositions using a (a) KG3 and (b) KG2 filtered Si solar cell as the reference cell. Calculations use the EQE spectra reported in Figure S6 for films with a 6% $Pb(SCN)_2$ excess and 10% SnF_2 excess relative to PbI_2 and SnI_2, respectively.

Spectral Mismatch of Devices without Pb(SCN)₂
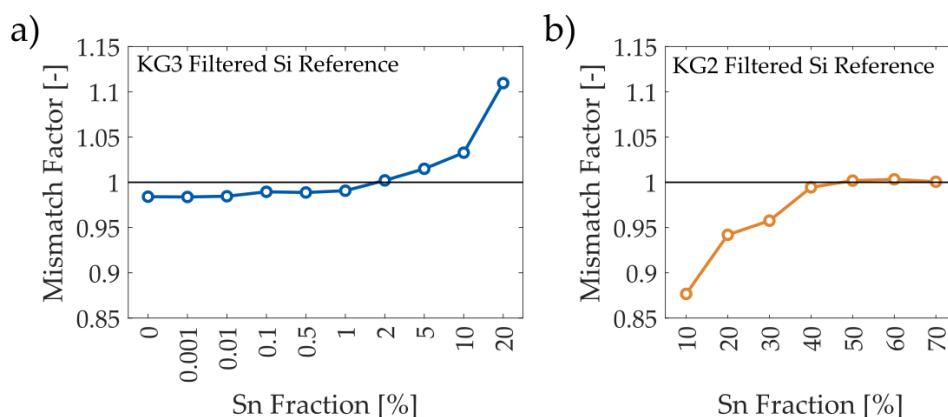
Figure S10. Spectral mismatch factor calculated for $(FA_{0.83}Cs_{0.17})(Pb_{1-y}Sn_y)I_3$ compositions using a (a) KG3 and (b) KG2 filtered Si solar cell as the reference cell. Calculations use the EQE spectra reported in Figure S7 for films without $Pb(SCN)_2$ addition and 10% SnF_2 excess relative to PbI_2 and SnI_2, respectively.

Table S1. Spectral mismatch factor calculated for $(FA_{0.83}Cs_{0.17})(Pb_{1-y}Sn_y)I_3$ compositions using a certified KG3 and KG2 filtered Si solar cell as the reference cell. Calculations use the EQE spectra reported in Figure S6-S7 for films with a 10% SnF_2 excess relative to SnI_2 and a 0% or 6% $Pb(SCN)_2$ excess relative to PbI_2.

Sn [%]	Spectral Mismatch Factor [-]				Mismatch Correction in Solar Simulator Calibration				Overall Mismatch Factor [-]			
	KG3 Filtered Si Ref		KG2 Filtered Si Ref		1.57 eV SS Calibration		1.30 eV SS Calibration		KG3 Filtered Si Ref		KG2 Filtered Si Ref	
	0% SCN	6% SCN	0% SCN	6% SCN	0% SCN	6% SCN	0% SCN	6% SCN	0% SCN	6% SCN	0% SCN	6% SCN
0	0.9878	0.9874			1.0038	1.0065			0.9841	0.9810		
0.001	0.9875	0.9897			1.0038	1.0065			0.9838	0.9833		
0.01	0.9883	0.9898			1.0038	1.0065			0.9846	0.9834		
0.1	0.9932	0.9902			1.0038	1.0065			0.9894	0.9838		
0.5	0.9925	0.9877			1.0038	1.0065			0.9887	0.9813		
1	0.9944	0.9897			1.0038	1.0065			0.9906	0.9833		
2	1.0059	0.9907			1.0038	1.0065			1.0021	0.9843		
5	1.0188	1.0014			1.0038	1.0065			1.0149	0.9949		
10	1.0366	1.0244			1.0038	1.0065			1.0327	1.0178		
20	1.1138	1.0667			1.0038	1.0065			1.1096	1.0598		
30			0.9947	0.9765			1.0388	1.0358			0.9575	0.9427
40			1.0330	1.0154			1.0388	1.0358			0.9944	0.9803
50			1.0407	1.0370			1.0388	1.0358			1.0018	1.0012
60			1.0422	1.0320			1.0388	1.0358			1.0033	0.9963
70			1.0394	1.0456			1.0388	1.0358			1.0006	1.0095

The spectrum of the solar simulator lamp was measured using a MAYA Pro (Ocean Optics) spectrophotometer equipped with a cosine corrector on the optical fibre. The measured spectrum was corrected for spectral sensitivity of the spectrophotometer by using a certified calibration lamp. The spectrum was converted into absolute spectral irradiance by measuring the current generated by a certified Si reference cell equipped with either a KG3 (for 0% Sn calibration) or KG2 filter (for 50% Sn calibration). Two calibrations were made for the solar simulator, one for a 1.57 eV ($MAPbI_3$) solar cell and another for a 1.30 eV ($(FA_{0.83}Cs_{0.17})(Pb_{0.5}Sn_{0.5})I_3$) solar cell using the method described by Snaith[8], where the lamp intensity of the solar simulator is adjusted to correct for the mismatch between the 1.30 or 1.57 eV perovskite solar cell and the corresponding Si reference cell (KG2 or KG3 filtered). The final calibration is such that the 1.30 or 1.57 eV perovskite solar cell would produce the same current in the solar simulator as it would in the AM1.5G solar spectrum.

$(FA_{0.83}Cs_{0.17})(Pb_{1-y}Sn_y)I_3$ perovskite solar cells were either tested in the 1.57 eV (0-20% Sn) or 1.30 eV (30-70% Sn) solar simulator calibration settings. The left columns in Table S1 report the calculated spectral mismatch factor for a perovskite solar cell with a given Sn composition and SCN content, which was determined[8] using its measured EQE and the appropriate Si reference cell listed in Table S1. The overall mismatch factor (right columns of Table S1) is then the calculated spectral mismatch factor for a given composition (left columns of Table S1) divided by the mismatch factor used in the solar simulator calibration (middle columns of Table S1). The overall mismatch factor is essentially the equivalent number of suns that illuminated a given solar cell during testing with the solar simulator. Therefore, the power conversion efficiencies measured with the solar simulator are corrected by dividing the measured value by the overall mismatch factor.

Photovoltaic Performance Metrics
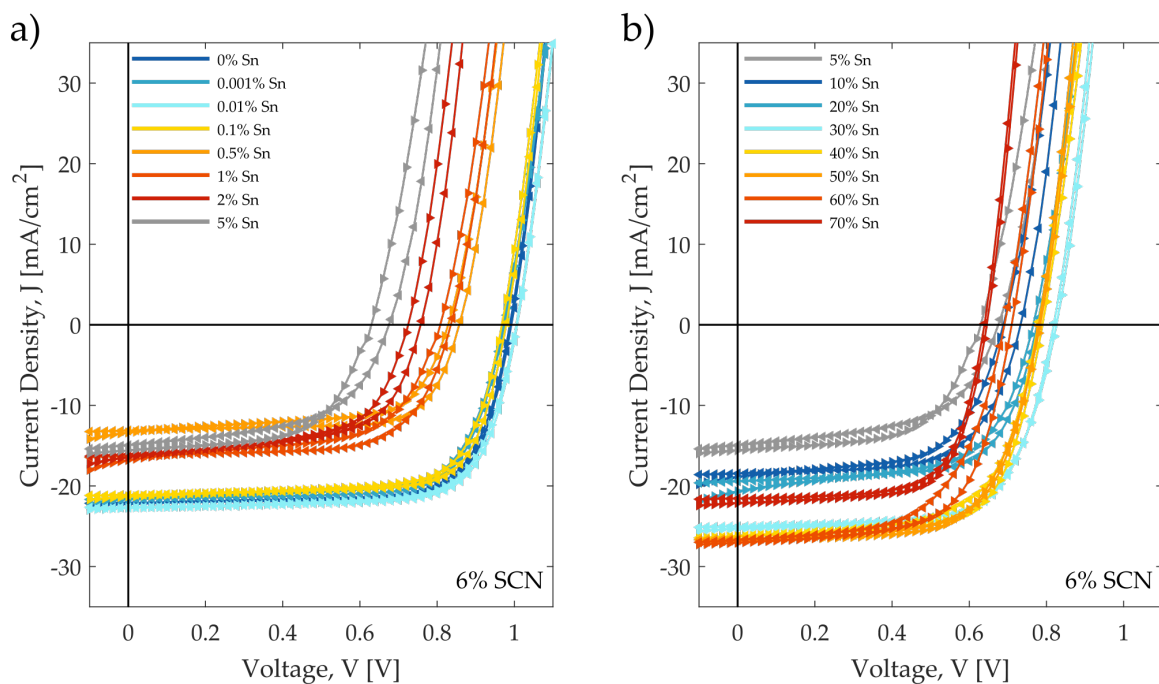
Figure S11. Champion current voltage characteristics for $(FA_{0.83}Cs_{0.17})(Pb_{1-y}Sn_y)I_3$ solar cells with (a) low Sn content (Sn Fraction = 0% to 5%) and (b) high Sn content (Sn Fraction = 5% to 70%). Each composition was fabricated with a 10% molar excess of SnF_2 over SnI_2 and 6% molar excess of $Pb(SCN)_2$ over PbI_2.
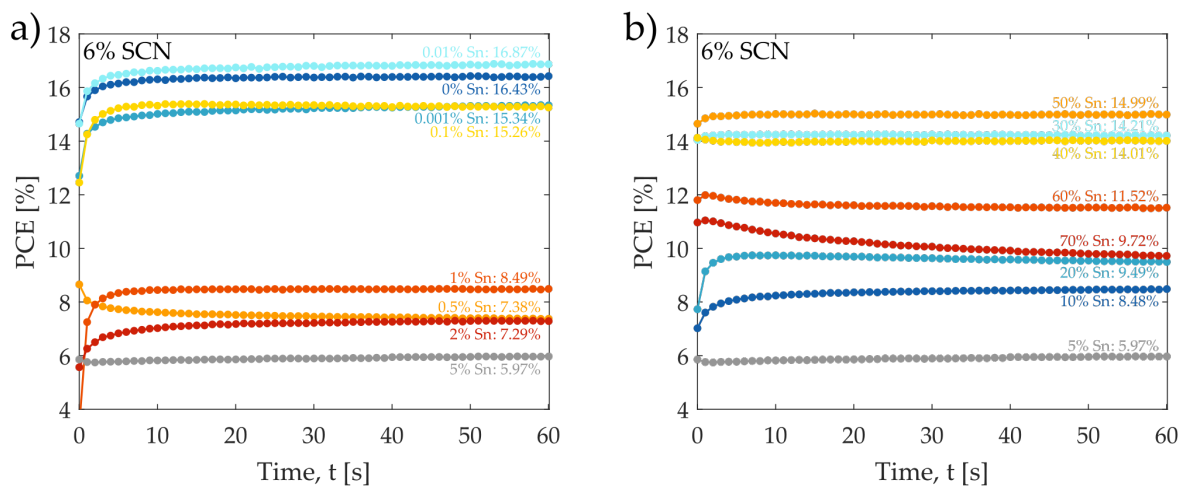
Figure S12. Power conversion efficiency time traces for $(FA_{0.83}Cs_{0.17})(Pb_{1-y}Sn_y)I_3$ solar cells with (a) low Sn content (Sn Fraction = 0% to 5%) and (b) high Sn content (Sn Fraction = 5% to 70%). Each composition was fabricated with a 10% molar excess of SnF_2 over SnI_2 and 6% molar excess of $Pb(SCN)_2$ over PbI_2.
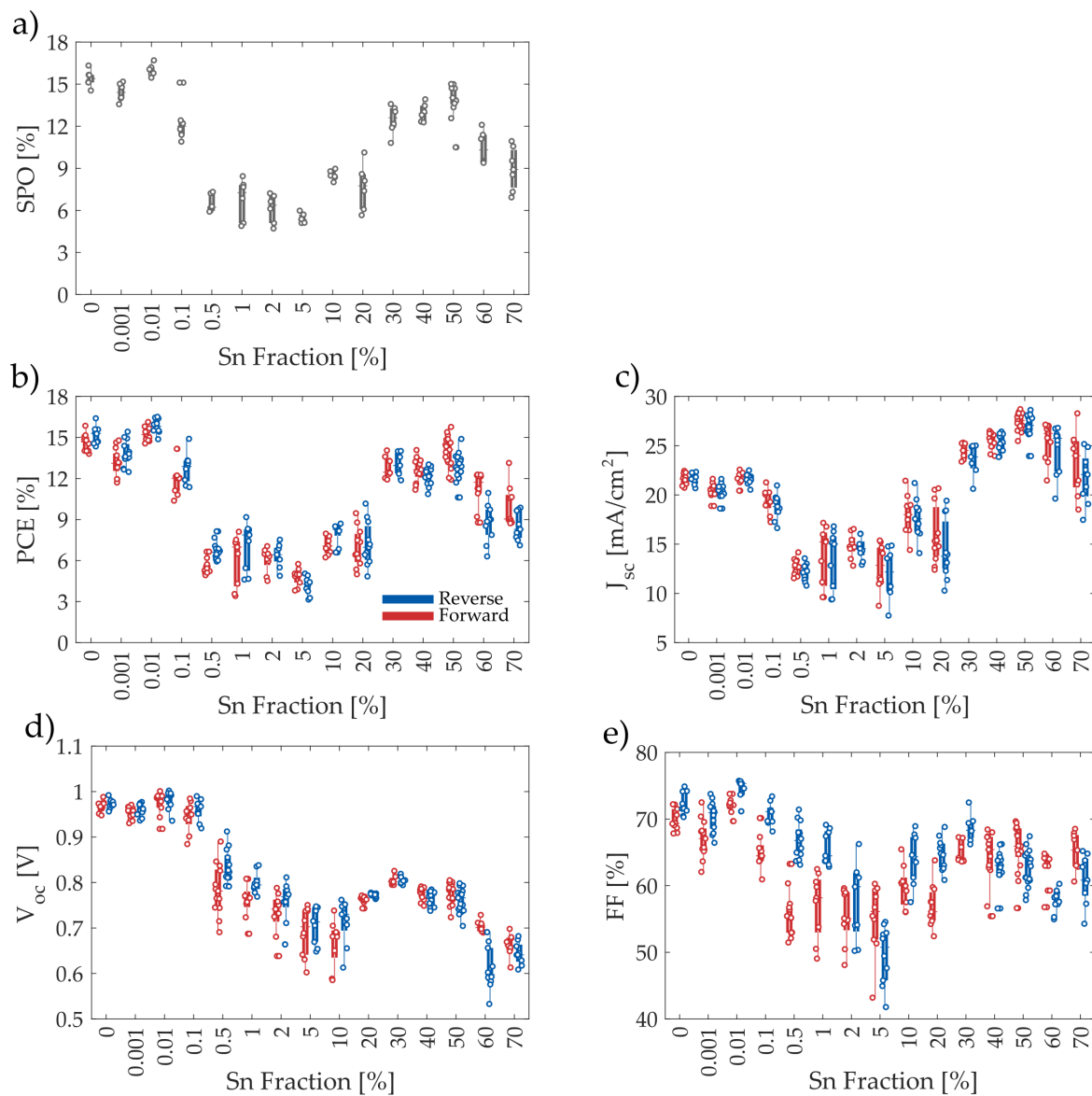
Figure S13. Compositional dependence of (a) steady-state power output (SPO) and (b-e) photovoltaic performance metrics as determined from the forward (in direction of short-circuit to open-circuit) and reverse (in direction of open-circuit to short-circuit) current-voltage characteristics. Note that the short-circuit current density, J_{sc}, values have also been corrected for spectral mismatch to allow for valid comparison across compositions when illuminated with an equivalent 1 sun irradiance under the AM1.5G spectrum.

Table S2. Summary of mean photovoltaic performance metrics and steady-state power output (SPO) for $(FA_{0.83}Cs_{0.17})(Pb_{1-y}Sn_y)I_3$ solar cells for each metal composition with 10% molar excess of SnF_2 over SnI_2 and 6% molar excess of $Pb(SCN)_2$ over PbI_2. Error corresponds to standard deviation and the champion metric is given in parentheses.

Sn Fraction (%)	PCE (%)		J_{sc} $\left(\frac{mA}{cm^2}\right)$		V_{oc} (V)		FF (%)		SPO (%)
	Forward	Reverse	Forward	Reverse	Forward	Reverse	Forward	Reverse	
0%	14.6 ± 0.7 (15.9)	15.2 ± 0.6 (16.4)	21.6 ± 0.6 (22.2)	21.6 ± 0.6 (22.2)	0.97 ± 0.01 (0.99)	0.97 ± 0.01 (0.99)	69.9 ± 1.6 (72.2)	72.2 ± 1.6 (74.9)	15.4 ± 0.6 (16.4)
0.001%	13.1 ± 1.0 (14.8)	13.8 ± 0.9 (15.4)	20.5 ± 0.7 (21.6)	20.4 ± 0.7 (21.6)	0.95 ± 0.01 (0.97)	0.96 ± 0.01 (0.97)	67.0 ± 2.8 (70.4)	70.4 ± 2.2 (73.2)	14.4 ± 0.6 (15.3)
0.01%	15.2 ± 0.5 (16.4)	15.8 ± 0.5 (16.9)	21.7 ± 0.6 (22.7)	21.6 ± 0.5 (22.7)	0.97 ± 0.03 (1.01)	0.98 ± 0.02 (1.01)	72.0 ± 1.1 (72.0)	74.6 ± 1.4 (73.8)	16.0 ± 0.4 (16.9)
0.1%	11.9 ± 1.1 (14.8)	12.8 ± 1.1 (15.4)	19.3 ± 1.3 (21.3)	18.8 ± 1.3 (21.1)	0.94 ± 0.03 (0.97)	0.96 ± 0.02 (0.98)	65.1 ± 2.6 (71.7)	70.7 ± 1.7 (74.5)	12.3 ± 1.5 (15.3)
0.5%	5.5 ± 0.5 (7.2)	6.7 ± 0.6 (8.2)	12.6 ± 0.8 (13.3)	12.1 ± 0.8 (13.1)	0.78 ± 0.06 (0.83)	0.83 ± 0.04 (0.86)	55.6 ± 3.4 (64.8)	66.7 ± 2.7 (72.7)	6.4 ± 0.6 (7.4)
1%	6.1 ± 1.8 (8.1)	7.1 ± 1.7 (9.2)	13.8 ± 3.0 (16.8)	13.5 ± 3.0 (16.3)	0.76 ± 0.04 (0.81)	0.80 ± 0.02 (0.84)	57.1 ± 4.9 (59.8)	65.7 ± 2.6 (67.4)	6.8 ± 1.5 (8.5)
2%	6.1 ± 0.9 (7.1)	6.4 ± 0.8 (7.5)	14.9 ± 1.2 (16.4)	14.5 ± 1.1 (16.1)	0.73 ± 0.05 (0.72)	0.76 ± 0.04 (0.76)	55.5 ± 4.1 (59.3)	57.8 ± 5.7 (61.9)	6.1 ± 1.0 (7.3)
5%	4.8 ± 0.6 (5.8)	4.2 ± 0.6 (5.6)	12.7 ± 2.2 (15.5)	12.0 ± 2.4 (15.0)	0.69 ± 0.05 (0.63)	0.72 ± 0.04 (0.68)	55.1 ± 5.2 (59.3)	49.6 ± 4.4 (55.4)	5.4 ± 0.3 (6.0)
10%	7.1 ± 0.7 (7.8)	8.0 ± 0.8 (8.7)	18.1 ± 2.1 (18.9)	17.7 ± 2.1 (18.5)	0.67 ± 0.05 (0.69)	0.71 ± 0.05 (0.73)	59.8 ± 3.2 (60.4)	63.9 ± 3.7 (64.3)	8.5 ± 0.3 (9.0)
20%	6.9 ± 1.4 (9.5)	7.2 ± 1.6 (10.2)	16.0 ± 3.0 (20.7)	14.4 ± 3.0 (19.4)	0.76 ± 0.01 (0.77)	0.77 ± 0.00 (0.78)	56.9 ± 3.2 (59.8)	64.8 ± 2.4 (67.5)	7.7 ± 1.7 (10.1)
30%	12.8 ± 0.8 (14.1)	13.0 ± 0.8 (14.0)	24.5 ± 0.8 (25.3)	23.6 ± 1.6 (25.0)	0.80 ± 0.01 (0.83)	0.80 ± 0.01 (0.82)	65.1 ± 1.6 (67.3)	68.7 ± 2.1 (68.3)	12.5 ± 1.0 (14.2)
40%	12.7 ± 0.9 (14.1)	12.2 ± 0.6 (13.0)	25.5 ± 0.8 (26.2)	25.2 ± 0.9 (26.2)	0.78 ± 0.01 (0.79)	0.77 ± 0.02 (0.78)	64.2 ± 4.1 (68.0)	63.0 ± 2.5 (63.8)	13.0 ± 0.6 (14.0)
50%	14.0 ± 1.1 (15.8)	12.9 ± 1.0 (14.9)	27.5 ± 0.9 (28.3)	27.1 ± 0.9 (27.8)	0.78 ± 0.02 (0.80)	0.76 ± 0.03 (0.79)	65.6 ± 3.5 (69.7)	62.4 ± 2.7 (67.4)	13.9 ± 1.3 (15.0)
60%	11.3 ± 1.3 (12.3)	8.7 ± 1.4 (10.9)	25.0 ± 2.0 (27.0)	24.6 ± 2.4 (26.7)	0.70 ± 0.01 (0.71)	0.61 ± 0.05 (0.69)	62.8 ± 2.6 (64.0)	57.7 ± 1.7 (59.2)	10.5 ± 1.2 (12.1)
70%	10.0 ± 1.5 (13.1)	8.5 ± 1.0 (9.9)	23.2 ± 3.2 (28.3)	21.7 ± 2.6 (25.2)	0.66 ± 0.02 (0.68)	0.64 ± 0.02 (0.64)	65.1 ± 2.8 (68.5)	60.9 ± 3.7 (60.8)	9.0 ± 1.5 (10.9)

X-ray Photoelectron Spectroscopy

Valence band (VB) and survey X-ray photoelectron spectroscopy (XPS) spectra were measured for samples with the following compositions: Sn = {0, 0.01, 0.1, 1, 10, 30, and 50%}. The valence band spectra show the same characteristic peak, the shape of which does not change with increasing Sn content. Assuming $E_F = 0$ eV, it is clear that with increasing Sn content there is a shift in the position of the VB onset towards the Fermi level (Figure S14a). The most pronounced shifts are observed in spectra corresponding to samples where Sn ≥ 1%. In the measured survey spectra, which we show in Figure S14b, we observe peaks characteristic of Sn in samples where Sn ≥ 1%. XPS typically provides

a resolution on the order of chemical ppm and a sample probe depth of up to 10 nm. We interpret the lack of Sn signal for the 0.01% and 0.1% samples as an indication that these atomic concentrations are below the detection limit of the instrument. If the Sn atoms are evenly distributed throughout the film at these low concentrations, they will be quite scarce with respect to all the other atoms in the region being probed near the surface.
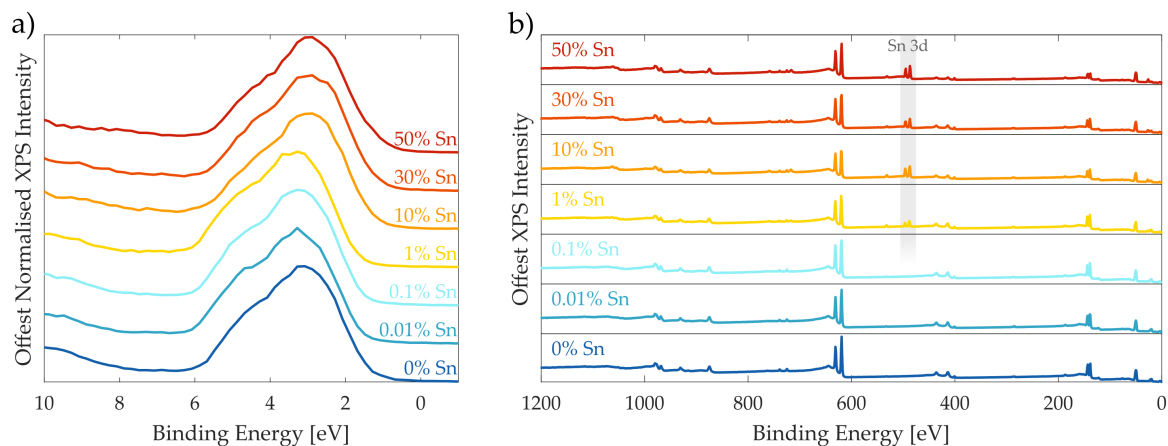
Figure S14. (a) Normalized X-ray photoelectron spectroscopy (XPS) spectra near the valence band edge and (b) XPS survey scan with the Sn $3d$ peaks highlighted around 486 eV.

Impact of Pb(SCN)$_2$ Addition on Photovoltaic Performance

We added a 6% molar excess of Pb(SCN)$_2$ to the perovskite precursor solutions because it boosts the performance and reproducibility of the lower band gap solar cells, as we show in Figure S15 (see Figures S16-S17 for the J-V characteristics and SPO traces and Table S3 for the mean and champion values when Pb(SCN)$_2$ is omitted).
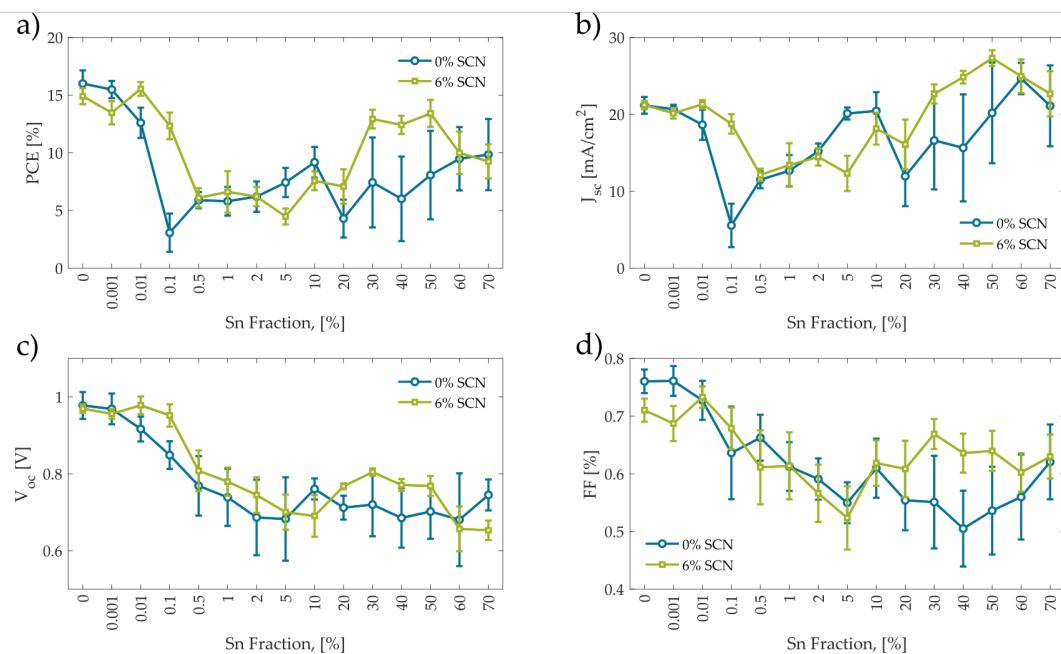
Figure S15. Mean (a) power conversion efficiency, (b) short-circuit current density, (c) open-circuit voltage, and (d) fill factor for (FA$_{0.83}$Cs$_{0.17}$)(Pb$_{1-y}$Sn$_y$)I$_3$ compositions prepared with either 0% or 6% Pb(SCN)$_2$ with respect to PbI$_2$ as a function of Sn fraction, defined by the molar percentage of SnI$_2$ to total metal iodide content in the perovskite precursor solution.

Photovoltaic Performance Metrics without Pb(SCN)$_2$
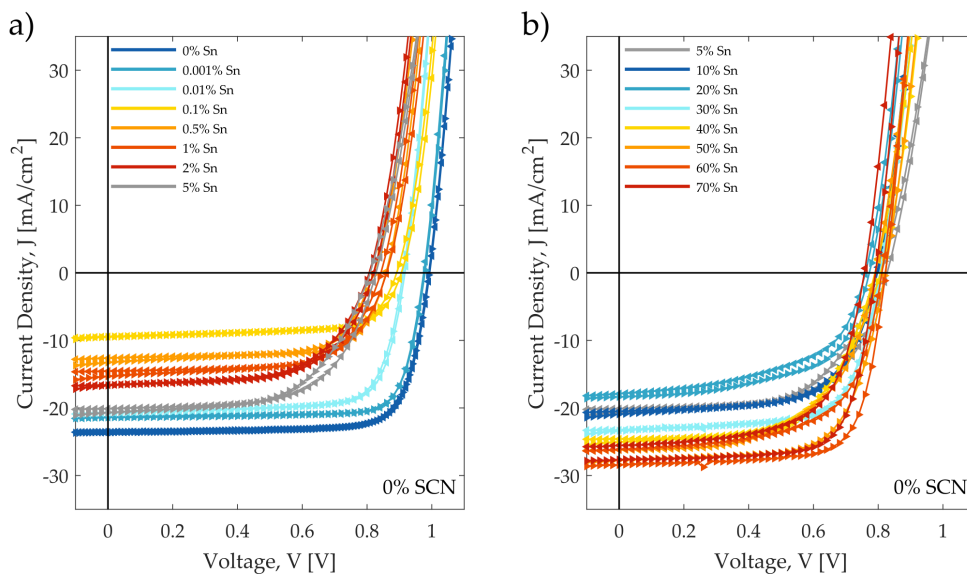
Figure S16. Champion current voltage characteristics for $(FA_{0.83}Cs_{0.17})(Pb_{1-y}Sn_y)I_3$ solar cells with (a) low Sn content (Sn Fraction = 0% to 5%) and (b) high Sn content (Sn Fraction = 5% to 70%). Each composition was fabricated with a 10% molar excess of SnF$_2$ over SnI$_2$ and without Pb(SCN)$_2$.
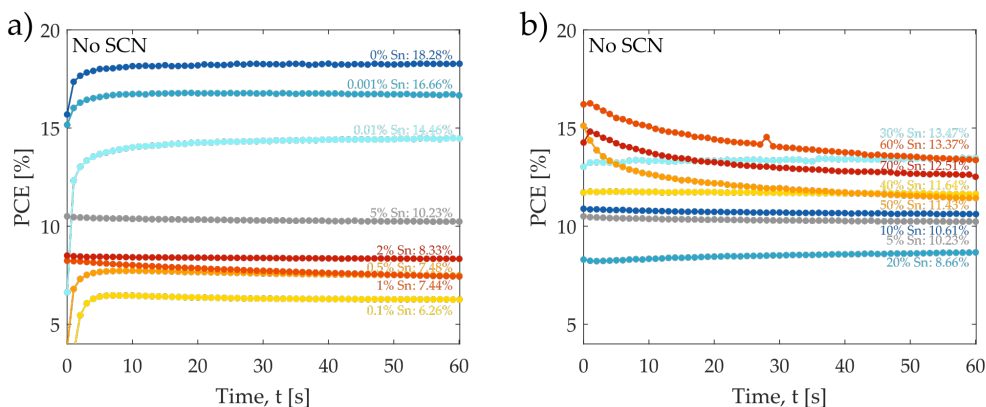
Figure S17. Power conversion efficiency time traces for $(FA_{0.83}Cs_{0.17})(Pb_{1-y}Sn_y)I_3$ solar cells with (a) low Sn content (Sn Fraction = 0% to 5%) and (b) high Sn content (Sn Fraction = 5% to 70%). Each composition was fabricated with a 10% molar excess of SnF$_2$ over SnI$_2$ and without Pb(SCN)$_2$.

Table S3. Summary of mean photovoltaic performance metrics and steady-state power ourput (SPO) for $FA_{0.83}Cs_{0.17}(Pb_{1-y}Sn_y)I_3$ solar cells for each metal composition with 10% molar excess of SnF_2 over SnI_2 and no $Pb(SCN)_2$ addition. Error corresponds to standard deviation and the champion metric is given in parentheses.

Sn (%)	PCE (%)		J_{sc} $\left(\frac{mA}{cm^2}\right)$		V_{oc} (V)		FF (%)		SPO (%)
	Forward	Reverse	Forward	Reverse	Forward	Reverse	Forward	Reverse	
0%	16.0 ± 1.1 (18.1)	16.0 ± 1.2 (18.2)	21.2 ± 1.1 (21.2)	21.2 ± 1.1 (23.5)	0.98 ± 0.04 (1.02)	0.98 ± 0.03 (1.03)	76.1 ± 1.7 (79.0)	76.0 ± 2.4 (80.3)	16.1 ± 0.8 (18.3)
0.001%	15.5 ± 0.8 (16.7)	15.5 ± 0.8 (16.7)	20.6 ± 0.7 (21.8)	20.7 ± 0.5 (21.7)	0.97 ± 0.04 (1.01)	0.97 ± 0.04 (1.01)	76.5 ± 2.1 (79.6)	75.7 ± 3.0 (80.3)	15.6 ± 0.5 (16.7)
0.01%	12.5 ± 1.4 (12.4)	12.7 ± 1.2 (14.4)	18.9 ± 1.8 (21.1)	18.4 ± 2.1 (20.8)	0.91 ± 0.03 (0.96)	0.92 ± 0.03 (0.96)	71.4 ± 3.2 (75.0)	74.1 ± 3.1 (78.7)	12.6 ± 1.7 (14.5)
0.1%	2.9 ± 1.7 (5.9)	3.2 ± 1.7 (6.0)	5.6 ± 2.9 (10.2)	5.5 ± 2.9 (10.0)	0.84 ± 0.04 (0.91)	0.86 ± 0.04 (0.92)	58.0 ± 6.4 (69.2)	69.3 ± 4.8 (80.0)	3.5 ± 2.2 (6.3)
0.5%	5.6 ± 0.7 (7.2)	6.2 ± 0.6 (7.8)	11.6 ± 1.1 (13.3)	11.4 ± 1.2 (13.2)	0.76 ± 0.08 (0.88)	0.78 ± 0.07 (0.87)	63.7 ± 2.3 (68.2)	68.8 ± 3.6 (73.1)	6.2 ± 0.8 (7.5)
1%	5.5 ± 1.3 (8.2)	6.1 ± 1.2 (8.4)	12.8 ± 2.1 (15.7)	12.5 ± 2.0 (15.5)	0.72 ± 0.08 (0.84)	0.75 ± 0.07 (0.86)	58.7 ± 3.4 (63.2)	63.9 ± 3.3 (68.6)	5.9 ± 1.1 (7.5)
2%	5.8 ± 1.3 (8.1)	6.6 ± 1.3 (8.9)	15.2 ± 1.0 (17.0)	15.2 ± 1.0 (16.8)	0.66 ± 0.11 (0.82)	0.71 ± 0.09 (0.83)	57.7 ± 2.9 (64.1)	60.5 ± 3.8 (67.9)	5.9 ± 2.3 (8.4)
5%	7.0 ± 1.3 (9.8)	7.9 ± 1.1 (10.5)	20.1 ± 0.8 (21.0)	20.1 ± 0.8 (21.1)	0.66 ± 0.12 (0.82)	0.70 ± 0.09 (0.83)	53.6 ± 3.1 (58.6)	56.4 ± 3.5 (62.8)	7.6 ± 1.6 (10.3)
10%	9.0 ± 1.2 (10.4)	9.4 ± 1.4 (11.1)	20.6 ± 2.5 (23.6)	20.3 ± 2.5 (23.6)	0.76 ± 0.03 (0.80)	0.77 ± 0.02 (0.80)	59.8 ± 3.1 (64.9)	62.2 ± 5.3 (67.9)	10.2 ± 0.9 (10.6)
20%	4.7 ± 1.7 (8.3)	3.9 ± 1.5 (7.4)	12.8 ± 4.0 (20.4)	11.1 ± 3.7 (19.9)	0.72 ± 0.03 (0.77)	0.71 ± 0.03 (0.76)	56.0 ± 5.9 (67.7)	54.8 ± 4.5 (61.9)	5.8 ± 2.5 (8.7)
30%	7.5 ± 4.0 (12.9)	7.4 ± 3.9 (12.8)	16.8 ± 6.4 (23.5)	16.5 ± 6.5 (22.4)	0.72 ± 0.09 (0.81)	0.72 ± 0.08 (0.81)	54.6 ± 8.7 (68.6)	55.6 ± 7.6 (68.4)	10.6 ± 2.3 (13.5)
40%	6.1 ± 3.8 (12.0)	5.9 ± 3.6 (11.7)	15.9 ± 7.1 (25.1)	15.4 ± 7.0 (24.7)	0.69 ± 0.08 (0.81)	0.68 ± 0.07 (0.79)	50.1 ± 6.8 (60.1)	50.9 ± 6.5 (60.8)	7.2 ± 3.8 (11.7)
50%	8.6 ± 4.1 (15.4)	7.5 ± 3.5 (12.5)	20.5 ± 6.6 (27.8)	19.9 ± 6.6 (27.3)	0.72 ± 0.07 (0.82)	0.69 ± 0.07 (0.79)	53.3 ± 8.5 (70.4)	51.9 ± 6.3 (65.1)	10.3 ± 3.6 (11.4)
60%	10.9 ± 2.3 (17.1)	8.1 ± 2.5 (13.3)	25.1 ± 2.1 (28.5)	24.2 ± 2.0 (26.5)	0.72 ± 0.07 (0.82)	0.64 ± 0.15 (0.81)	59.8 ± 7.0 (73.3)	52.2 ± 5.7 (62.8)	9.4 ± 3.9 (13.4)
70%	11.1 ± 3.1 (15.9)	8.5 ± 2.7 (2.2)	21.9 ± 5.4 (27.7)	20.4 ± 5.4 (25.6)	0.77 ± 0.04 (0.81)	0.73 ± 0.03 (0.76)	66.7 ± 4.5 (72.5)	57.5 ± 4.6 (63.1)	9.6 ± 3.0 (12.5)

Material Properties of Perovskite without Pb(SCN)₂ Addition

The addition of $Pb(SCN)_2$ does impact several material properties of the perovskite thin-films when the Sn content is less than 20%. First of all, as we infer from XRD, it generates two impurity phases, PbI_2 and δ-$CsPbI_3$, which is consistent with previous reports for (FA:Cs)PbI_3 systems.[9] Both of these phases have been identified here by their XRD peaks (Figure S5) in compositions with a Sn fraction of 20% or less, whereas only the PbI_2 impurity exists for Sn fractions between 30%-50%. The apparent high strength of PbI_2 peak at $2\theta \sim 12.6°$ for the low Sn composition (Figure S5) is due to the high degree of preferred orientation of the impurity phase with the c-axis normal to the substrate. For the 0% Sn composition, the ratio of the intensities for the [001]/[100] PbI_2 reflections is ~75 rather than ~2, which is expected for a powder sample.[10] Scanning electron micrographs (Figure S1) show a perovskite

19

morphology that is perforated with both rods and lighter-contrast platelets, which have been previously identified by Yu *et al* as PbI_2 and δ-$CsPbI_3$ in $(FA_{0.8}Cs_{0.2})PbI_3$.[9] When $Pb(SCN)_2$ is absent from the perovskite solution, the PbI_2 content is substantially reduced and we do not observe the δ-$CsPbI_3$ phase in the powder XRD patterns (Figure S18) regardless of the metal composition. Secondly, compared to the thin-films where $Pb(SCN)_2$ has been omitted (Figure S19), a 6% molar excess tends to produce thin-films with larger grains (Figure S1) when the Sn fraction is less than 30%, which is also consistent with previous reports for neat Pb materials.[9,11] Lastly, adding $Pb(SCN)_2$ changes the overall ratio of Pb:Sn in the film, which blue-shifts the optical band gap compared to films with the same PbI_2:SnI_2 precursor ratio where it has been omitted (Figure S3b, Figure S4b and Figure S20).

Powder X-ray Diffraction Patterns of Perovskite without $Pb(SCN)_2$
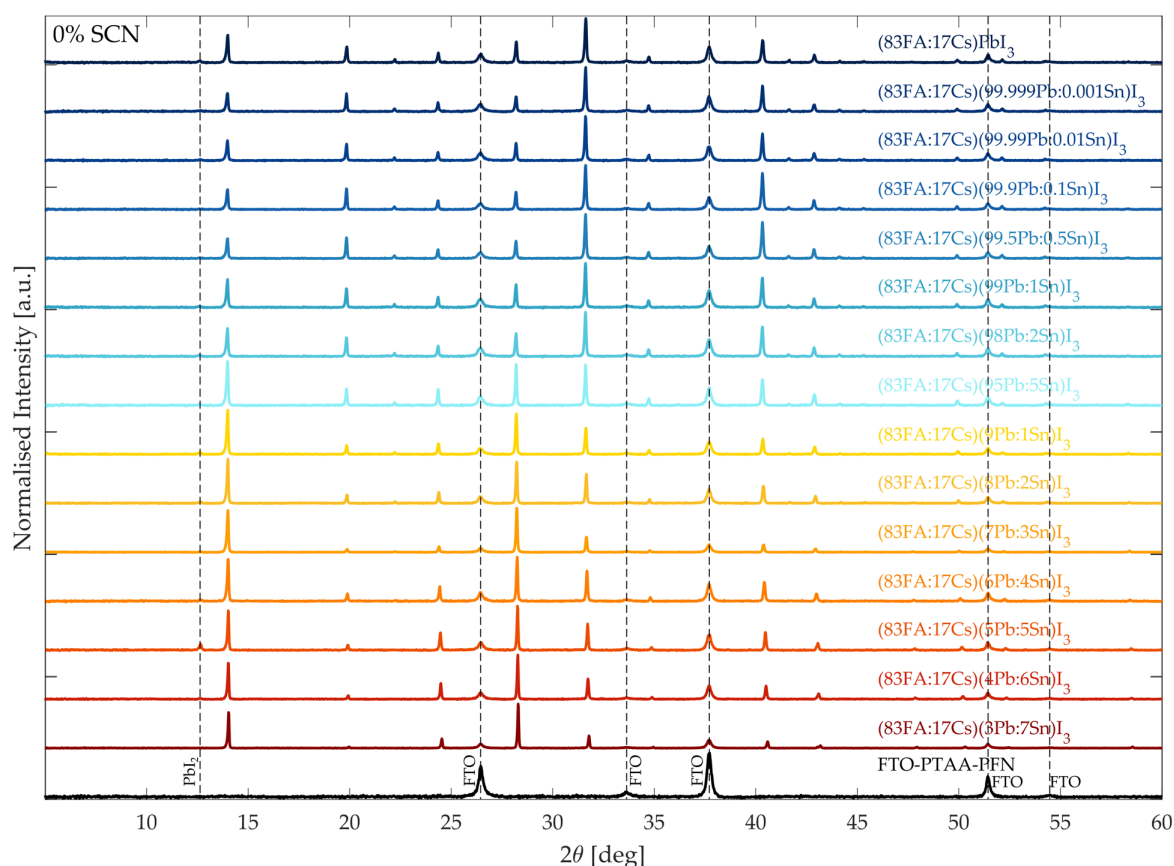
Figure S18. Powder X-ray diffractograms of $(FA_{0.83}Cs_{0.17})(Pb:Sn)I_3$ thin-films prepared on a FTO/PTAA/PFN stack. All films have are prepared with a 10% excess of SnF_2 with respect to the SnI_2 content and no $Pb(SCN)_2$ addition. Impurity phases of PbI_2 are indicated.

Scanning Electron Microscopy of Perovskite without Pb(SCN)$_2$
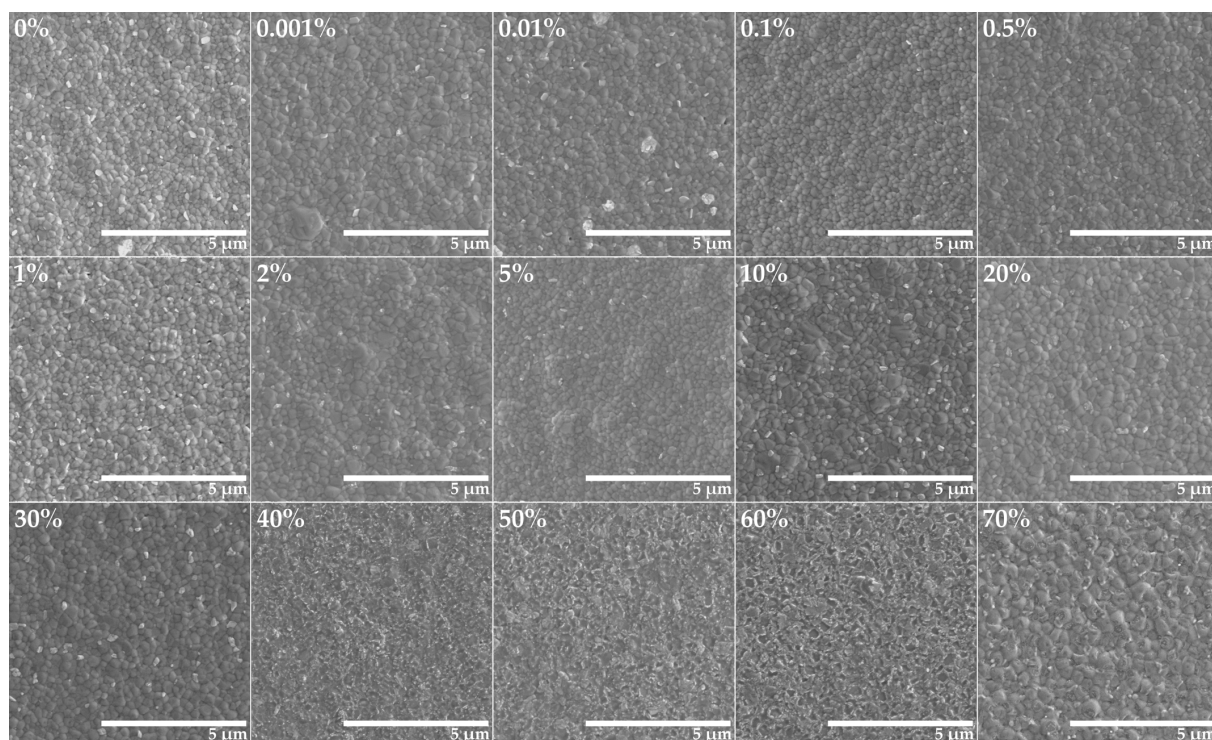
Figure S19. Scanning electron micrographs of $(FA_{0.83}Cs_{0.17})(Pb_{1-y}Sn_y)I_3$ with a 10% excess of SnF_2 with respect to the SnI_2 content and no added Pb(SCN)$_2$. The percentage of the metal iodide content that is Sn is written in the upper left corner of each panel.

Impact of Pb(SCN)$_2$ on Band Gap
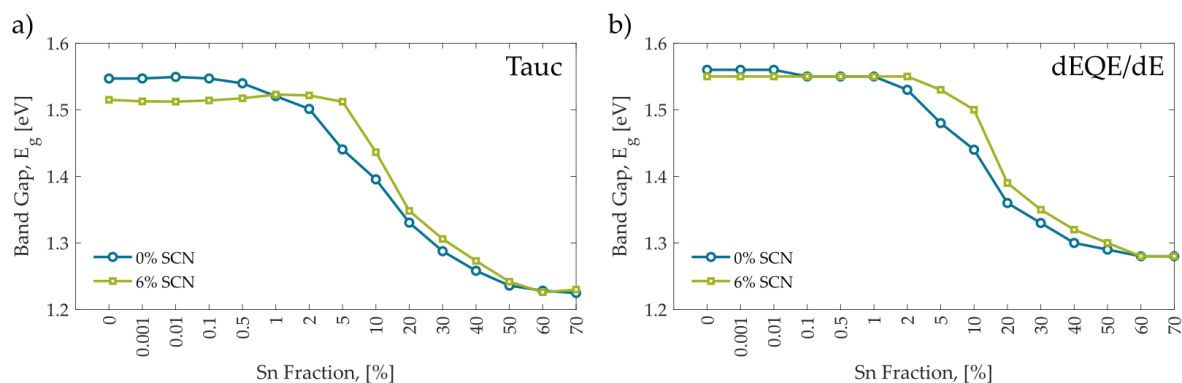
Figure S20. Influence of SCN addition on the band gap of $(FA_{0.83}Cs_{0.17})(Pb_{1-y}Sn_y)I_3$ as determined by the (a) Tauc plot and (b) the peak of the derivative of the measured EQE spectra with respect to photon energy.

Device Performance as a Function of Band Gap

Despite introducing impurities into the wider gap materials, Pb(SCN)$_2$ addition does not hinder photovoltaic performance in the wide band gap range and serves to greatly improve performance for the narrow band gap compositions. The exception is the neat Pb composition, which can achieve a steady-state power output of 18.3% without Pb(SCN)$_2$ (Figure S17a). Most importantly, when the performance metrics are plotted as a function of band gap (Figure S21), it becomes clear that the photovoltaic performance metrics overlay for the series with and without Pb(SCN)$_2$ when $E_g \geq 1.4$ eV. In this range the V_{oc}, J_{sc}, and PCE all drop precipitously as the band gap is narrowed regardless of

thiocyanate addition. These findings decouple the influence of Pb(SCN)$_2$ addition from metal content in the performance trends and demonstrate that the reductions in solar cell performance are not due to the additive and its associated impurity phases, but rather result from the incorporation of Sn itself into the perovskite film. Therefore, whilst Pb(SCN)$_2$ is helpful to improve performance in the low band gap regime (Sn ≥ 30%), it is not effective at mitigating the poor optoelectronic quality that is observed within the "defective zone" (0.5% ≤ Sn ≤ 20%). It is, however, helpful at improving the reproducibility of low band gap solar cells outside the "defective zone".
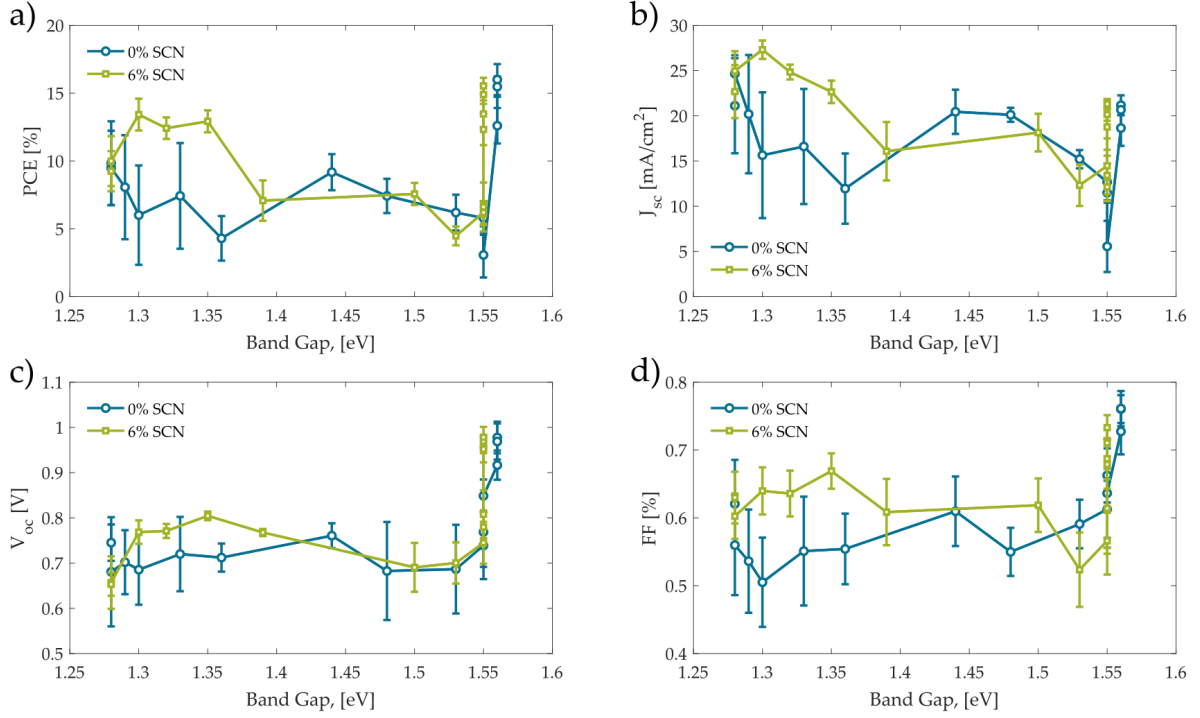
Figure S21. Mean (a) power conversion efficiency, (b) short-circuit current density, open-circuit voltage, and (d) fill factor for (FA$_{0.83}$Cs$_{0.17}$)(Pb$_{1-y}$Sn$_y$)I$_3$ compositions prepared with either 0% and 6% Pb(SCN)$_2$ with respect to PbI$_2$ as a function of band gap, defined by the Tauc plot of the absorption spectra.

Charge Carrier Mobility Calculation

The charge carrier mobility μ is given by

$$\mu = \frac{\Delta S A_{eff}}{Ne} \tag{S1}$$

where ΔS is the sheet conductivity of the perovskite thin film, A_{eff} is the effective area of the overlap of optical pump and THz probe pulse, N is the number of photoexcited charge carriers, and e is the elementary charge.

Assuming that the film thickness is much smaller than the THz wavelength, the sheet photoconductivity ΔS of a thin film between two media of refractive indices, n_A and n_B, can be expressed as[12–14]

$$\Delta S = -\varepsilon_0 c \left(n_A + n_B \right) \left(\frac{\Delta T}{T} \right) \tag{S2}$$

where $\Delta T/T$ is the experimentally determined change in transmitted THz electric field amplitude. In our experiment, $n_A = 1$ for vacuum and $n_B = 2.13$ for the z-cut quartz substrate.

The number of photo-excited charge carriers N can be determined using the following equation:

$$N = \varphi \frac{E\lambda}{hc}\left(1 - R_{pump}\right)\left(1 - T_{pump}\right)$$

<div align="right">S3</div>

where E is the energy contained in an optical excitation pulse of wavelength λ, R_{pump} is the reflectivity of the sample at normal incidence of the excitation beam, T_{pump} transmittance of the pump beam, and φ is the ratio of free charge carriers created per photons absorbed (the photon-to-charge branching ratio).

Substituting Equations S2 and S3 into Equation S1, the following equation is obtained:

$$\varphi\mu = -\varepsilon_0 c\left(n_A + n_B\right)\frac{A_{eff}hc}{E e\lambda\left(1 - R_{pump}\right)\left(1 - T_{pump}\right)}\left(\frac{\Delta T}{T}\right)$$

<div align="right">S4</div>

Because $0 \leq \varphi \leq 1$, the effective mobility $\varphi\mu$ represents a lower limit, which becomes identical to the actual mobility for full photon to free carrier conversion. To allow accurate determination of $\varphi\mu$, we ensured that excitation conditions were in the linear regime. It should also be noted that the determined charge carrier mobility arises from the contributions of both electrons and holes and that these contributions cannot be separated.

Photoluminescence Quantum Efficiency
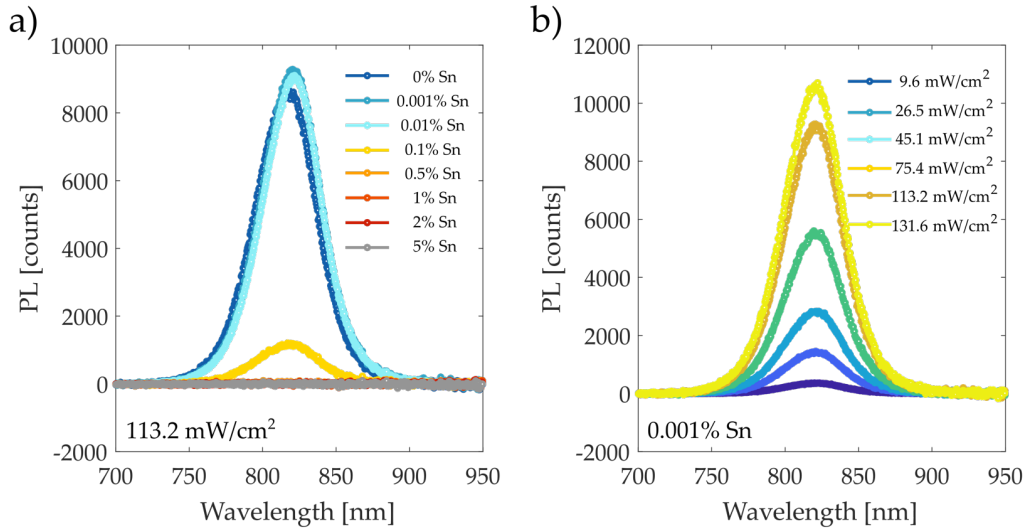
Figure S22. PL spectra collected by an integrating sphere for calculating the PLQE of encapsulated $(FA_{0.83}Cs_{0.17})(Pb_{1-y}Sn_y)I_3$ thin-films with (a) various Sn contents at 113.2 mW/cm^2 irradiance of a 520 nm laser and (b) various laser irradiances of a 520 nm laser on a samples with 0.001% Sn. All films contained a 10% excess of SnF$_2$ with respect to the SnI$_2$ content and a 6% excess of Pb(SCN)$_2$ with respect to the PbI$_2$ content.

Time-Resolved Photoluminescence Spectroscopy

The PL decay profile collected with time-correlated single photon counting (TCSPC) were fitted using the stretched-exponential model described by Equation S5:

$$PL = \alpha e^{\left(-\frac{t}{\tau_c}\right)^\beta} + \delta$$

<div align="right">S5</div>

$$\langle\tau\rangle = \frac{\tau_c}{\beta}\Gamma\left(\frac{1}{\beta}\right)$$

<div align="right">S6</div>

where Γ is the gamma function.

The PL lifetimes were estimated by the time it takes for the PL to reduce to $1/e$ of the original value, $\tau_{1/e}$. This was chosen over the $\langle\tau\rangle$ lifetime value often used in conjunction with the stretched-

exponential model because the behaviour of the films with Sn content greater than 0.1% is far from monomolecular, as is indicated by β values much less than 1 (Table S4). The $t_{1/e}$ lifetime values is a relevant choice to compare measurements regardless of Sn content.

Table S4. Fitting parameters (β, τ_c) of the TRPL data to a stretched exponential and the extracted values of PL lifetime ($\langle \tau \rangle$, $\tau_{1/e}$) for different Sn concentrations in FA$_{0.83}$Cs$_{0.17}$(Pb$_{1-y}$Sn$_y$)I$_3$ with a 10% excess of SnF$_2$ with respect to the SnI$_2$ content and a 6% excess of Pb(SCN)$_2$ with respect to the PbI$_2$ content.

Sn [%]	β [-]	τ_c [ns]	$\langle \tau \rangle$ [ns]	$t_{1/e}$ [ns]
0	7.783e-01	1.157e+03	1.337e+03	1133
0.001	8.135e-01	1.591e+03	1.782e+03	1437
0.01	8.308e-01	1.237e+03	1.366e+03	1159
0.1	8.335e-01	3.706e+02	4.082e+02	369.3
0.5	2.351e-01	3.868e-02	1.371e+00	13.5
1	2.287e-01	7.247e-03	3.096e-01	10.3
2	1.567e-01	1.462e-05	2.183e-02	8.6

Photothermal Deflection Spectroscopy

Urbach energy values were extracted from the absorbance spectra obtained with PDS by fitting the band edge to a linear exponential of the form:

$$\alpha = \alpha_0 e^{(E-E_g)/E_U} \tag{S7}$$

where E is the photon energy, E_g is the band gap, and E_U is the Urbach energy.[15]

We find that in the case of our unintentionally p-doped (FA$_{0.83}$Cs$_{0.17}$)(Pb$_{1-y}$Sn$_y$)I$_3$ system, the values for E_U extracted from the band edge using Equation S7 can be influenced substantially by the background of level due to free-carrier absorption. To illustrate this, we added to the measured absorbance spectrum for the neat Pb film (Figure S23a) a uniform background of 3e-2 (Figure S23b) in order to reach the background level measured for the 50% Sn sample (Figure S23c). When the band edge is fit to the linear exponential using Equation S1, we see that the Urbach energy rises from 18.9 meV for the measured neat Pb spectrum (Figure S23a) to 29.1 meV even though the absorbance spectrum is otherwise unchanged. Therefore, direct comparison of Urbach energies from PDS measurements across samples with different levels of background doping could lead to a misinterpretation that the more highly doped material is inherently more disordered.
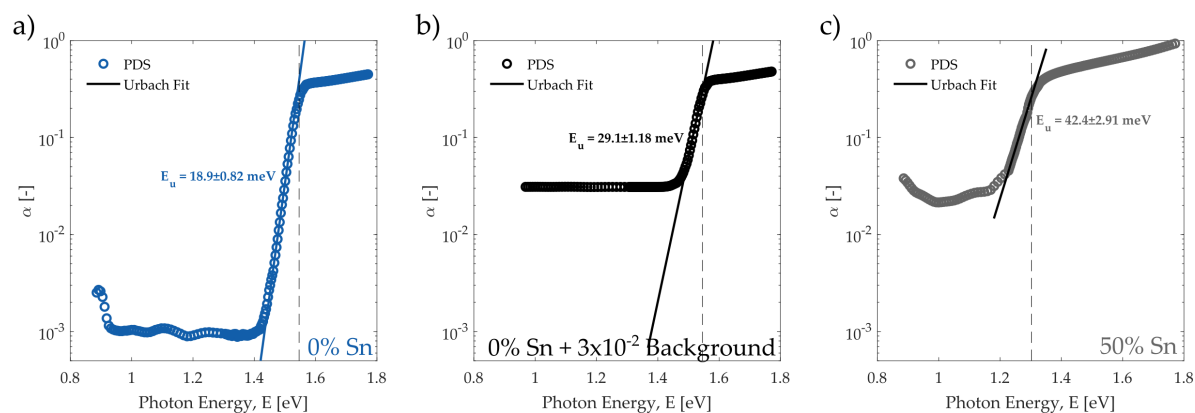
Figure S23. Absorbance spectra of perovskite thin-films with a metal composition of (a) 0% Sn, (c) 50% Sn as measured by photothermal deflection spectroscopy (PDS). (b) The absorbance spectrum measured for 0% Sn (shown in panel (a)) after a uniform background of 3×10⁻² has been added. The Urbach energy corresponding to the linear exponential fit (solid line) is printed in each panel.

Fourier-Transform Photocurrent Spectroscopy
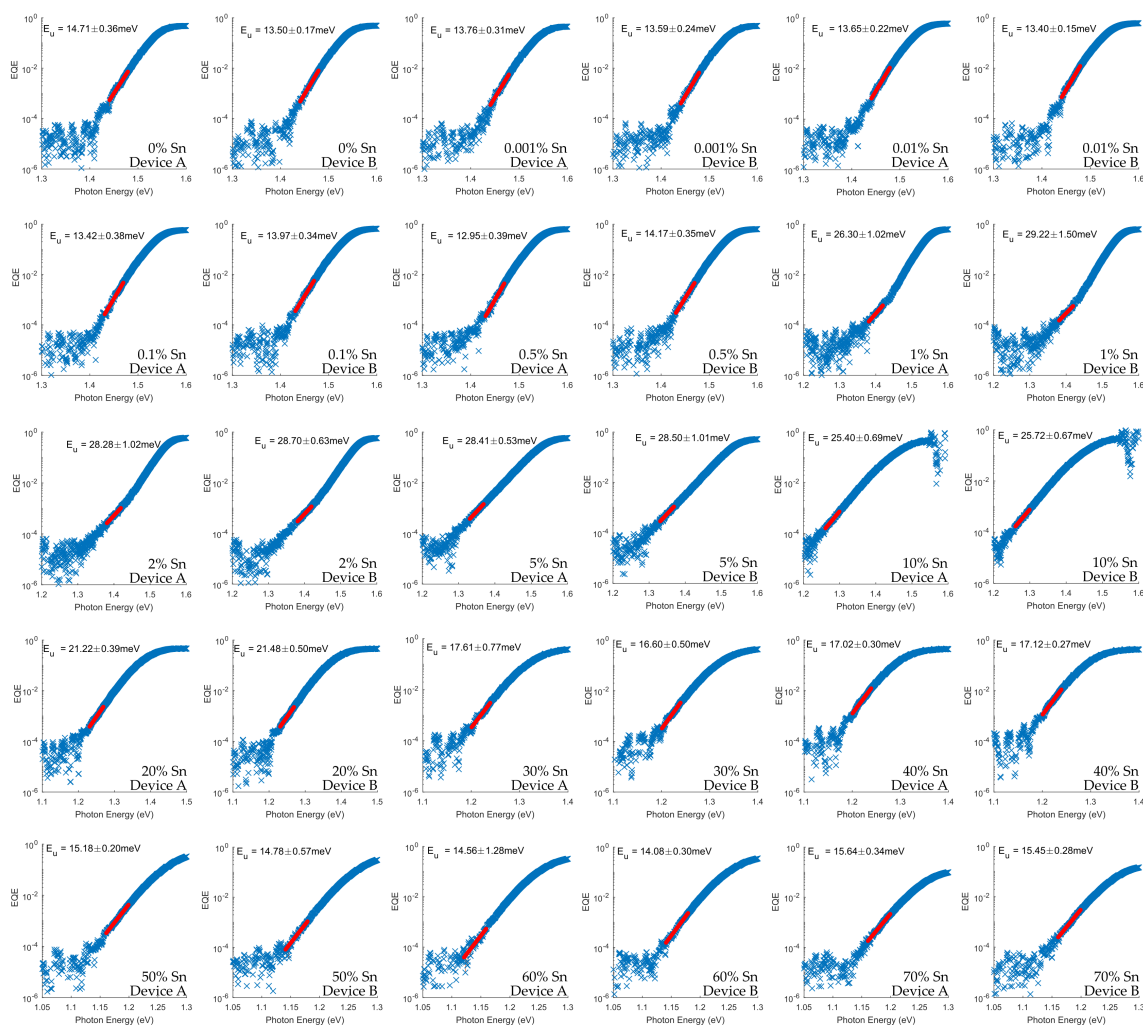
Figure S24. Urbach tails of the external quantum efficiency (EQE) spectra obtained using Fourier transform photocurrent spectroscopy (FTPS) for two representative devices for each Sn composition in the $FA_{0.83}Cs_{0.17}(Pb_{1-y}Sn_y)I_3$ series. The Urbach Energy (E_u) was determined by fitting a line (marked in red) to the Urbach tail. Each composition was fabricated with a 10% molar excess of SnF_2 over SnI_2 and 6% molar excess of $Pb(SCN)_2$ over PbI_2.

Photoluminescence Peak Fitting
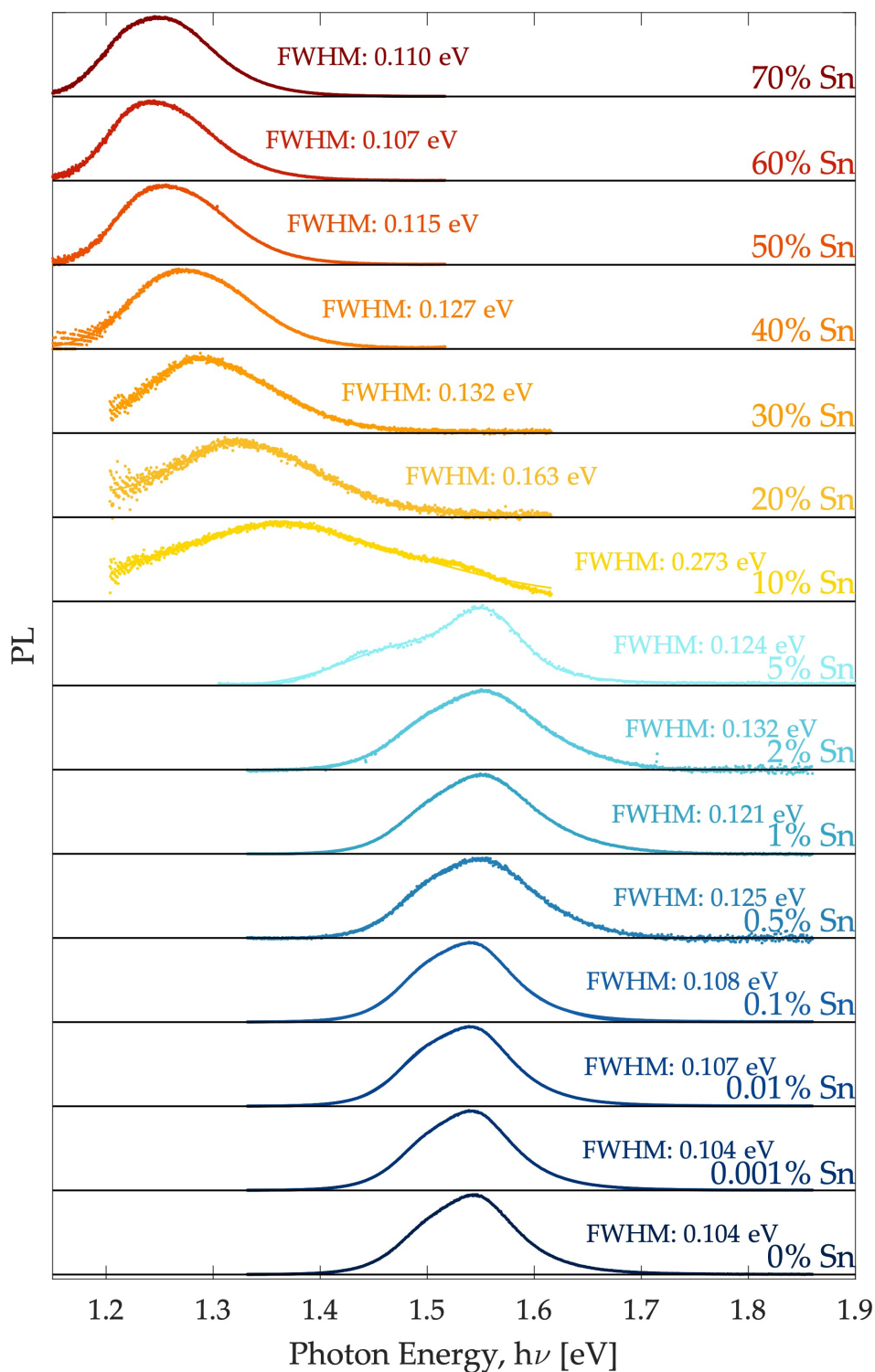
Figure S25. Photoluminescence (PL) peak measured for $(FA_{0.83}Cs_{0.17})(Pb_{1-y}Sn_y)I_3$ solar cells (indicated by circle markers) and the fitted peak by the superposition of three gaussians (solid lines). The FWHM is printed for each peak fit.

EQE Derivative Peak Fitting
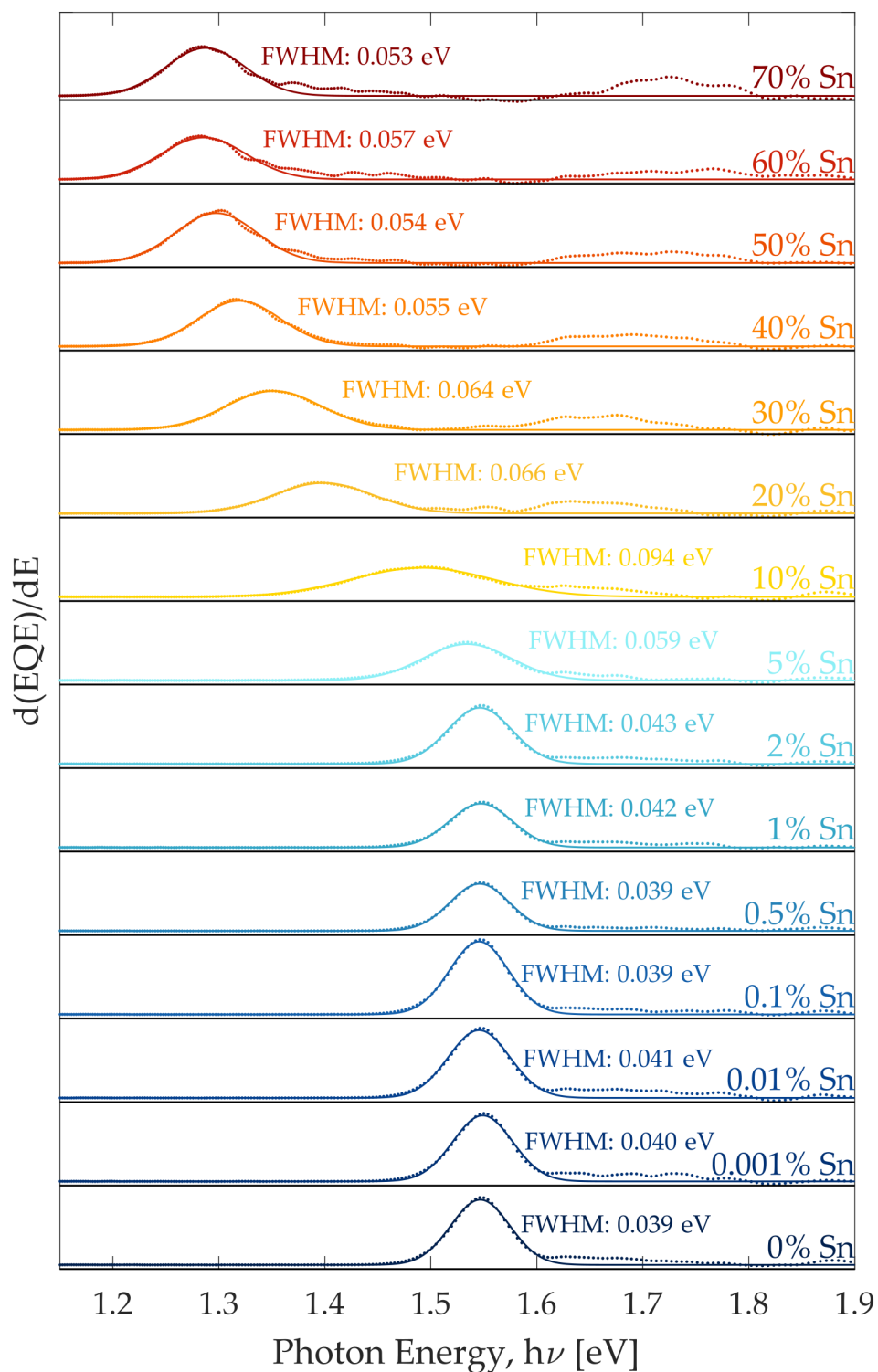
Figure S26. External quantum efficiency (EQE) derivative with respect to photon energy (E), $dEQE/dE$, measured for $(FA_{0.83}Cs_{0.17})(Pb_{1-y}Sn_y)I_3$ solar cells (dot markers) and the fitted Gaussian to the peak (solid lines). The FWHM is printed for each Gaussian fit.

Williamson-Hall Analysis
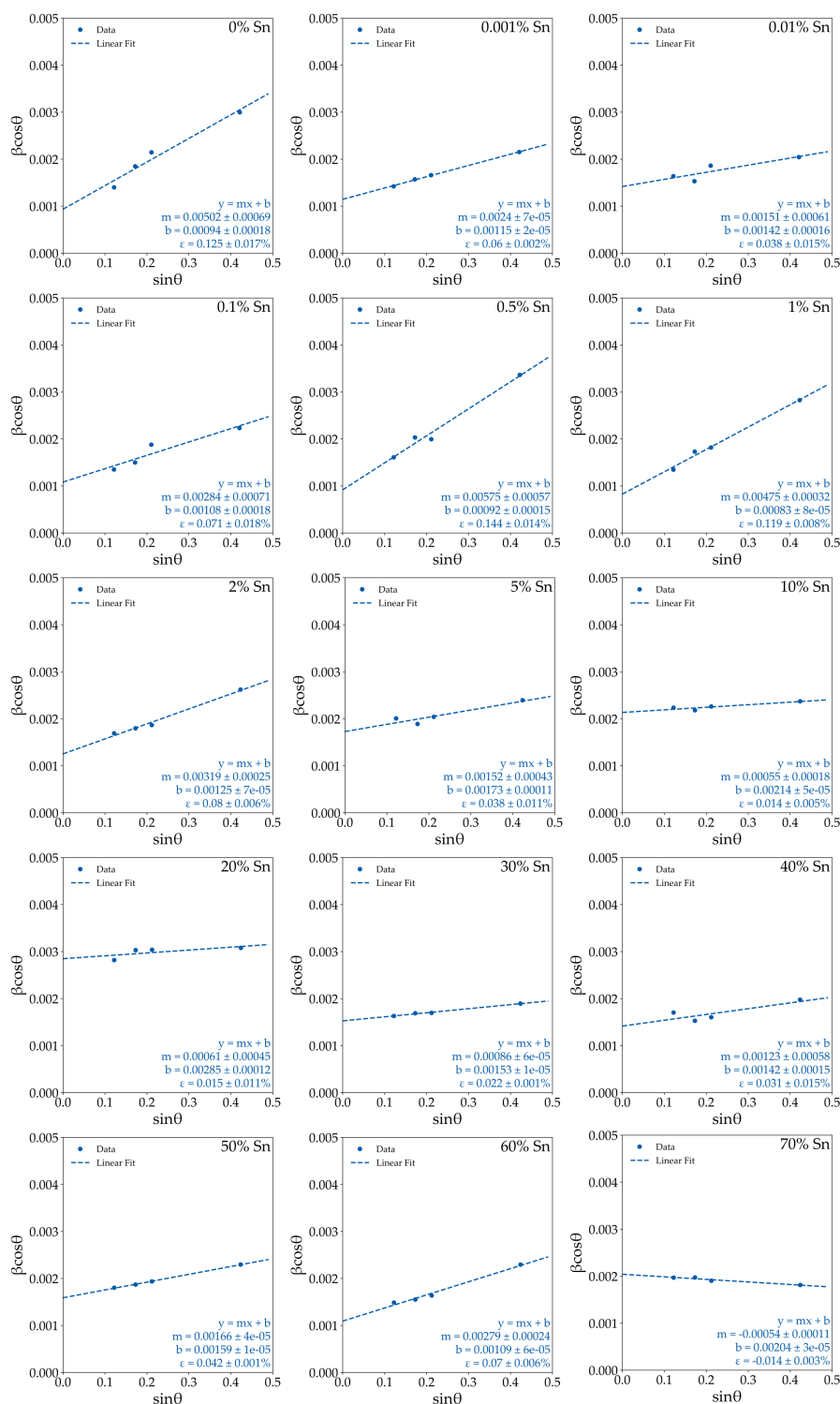
Figure S27. Williamson-Hall analysis where the specimen broadening, β, of several perovskite X-ray diffraction peaks presented in Figure S5 for each $(FA_{0.83}Cs_{0.17})(Pb_{1-y}Sn_y)I_3$ composition when 6% $Pb(SCN)_2$ excess is added relative to the PbI_2 concentration in the precursor solution. Note that ε is the microstrain, which is determined from the slope, m, of the linear fit ($\varepsilon = m/4$), and β has the units of radians.

Electroluminescence
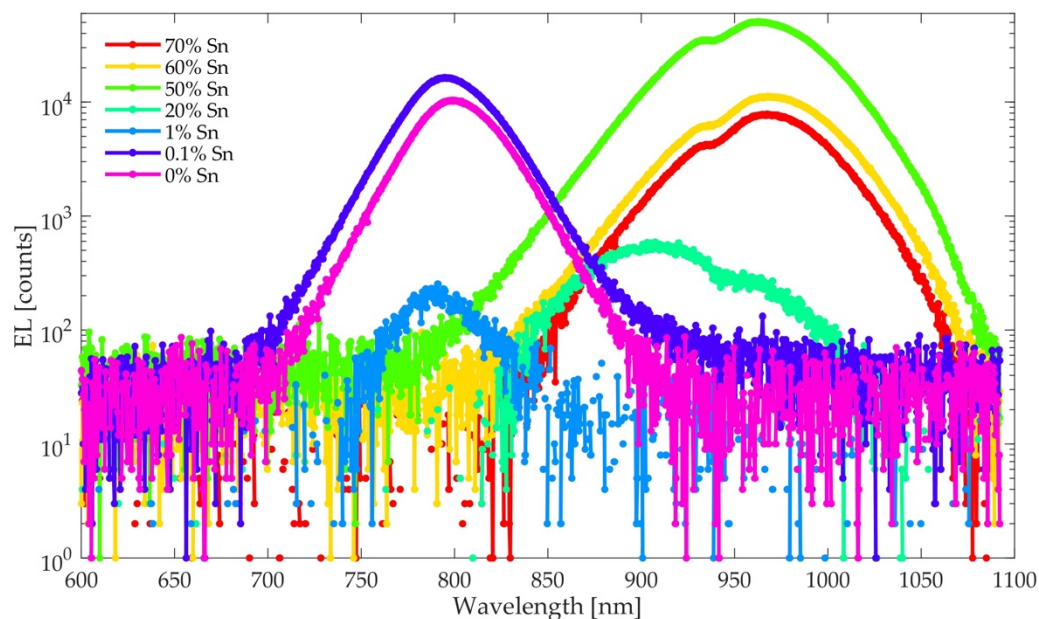
Figure S28. Electroluminescence spectra from (a) $(FA_{0.83}Cs_{0.17})(Pb_{1-y}Sn_y)I_3$ solar cells with various Sn fractions and (b) an optimised $(FA_{0.83}Cs_{0.17})(Pb_{0.7}Sn_{0.3})I_3$ solar cells with a 1.34 eV band gap.

Optimised 1.30 and 1.33 eV Band Gap Perovskites

1.33 eV External Quantum Efficiency
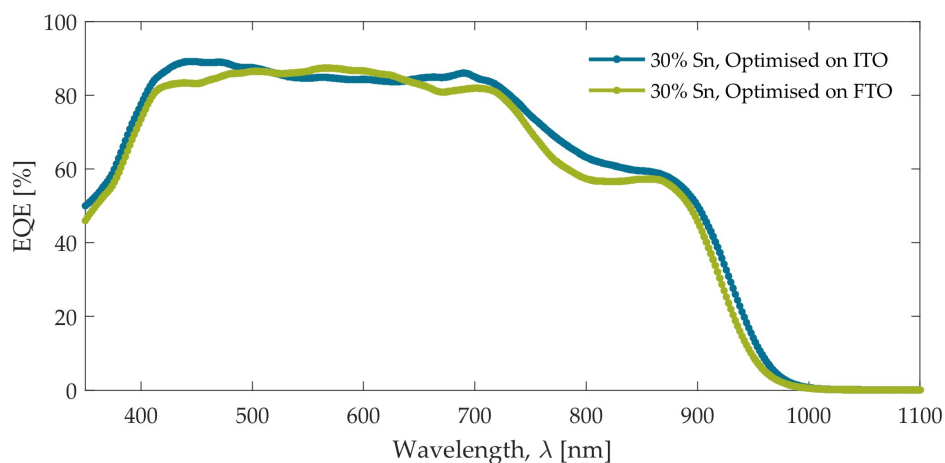
Figure S29. Comparison of external quantum efficiency (EQE) spectra for the optimised $(FA_{0.83}Cs_{0.17})(Pb_{0.7}Sn_{0.3})I_3$ composition prepared on either ITO/PTAA/PFN or FTO/PTAA/PFN. The perovskite precursor contained a 5% molar excess of $Pb(SCN)_2$ with respect to PbI_2 and 10% molar excess of SnF_2 with respect to SnI_2.

1.33 eV X-ray Diffraction
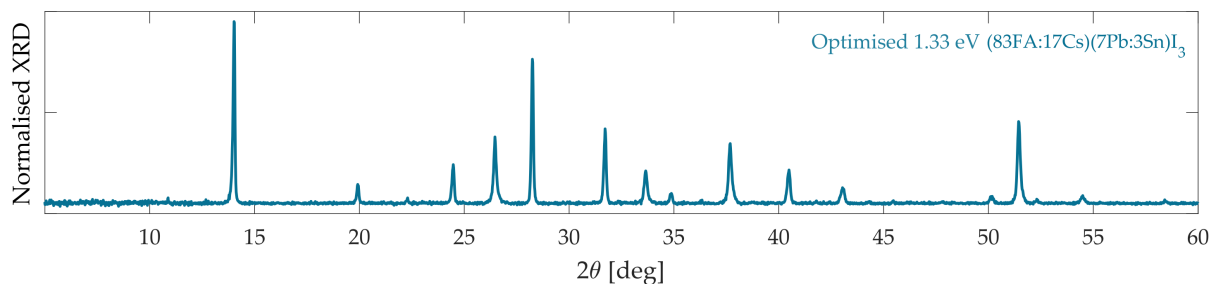
Figure S30. Powder XRD pattern for the optimised 1.33 eV band gap $(FA_{0.83}Cs_{0.17})(Pb_{0.7}Sn_{0.3})I_3$ composition prepared with a 5% molar excess of $Pb(SCN)_2$ with respect to PbI_2 and 10% molar excess of SnF_2 with respect to SnI_2. The perovskite film was prepared on the same half-stack used in optimised devices: ITO/PTAA/PFN

Photovoltaic Performance Metrics

Table S5. Summary of mean photovoltaic performance metrics for $(FA_{0.83}Cs_{0.17})(Pb_{0.7}Sn_{0.3})I_3$ solar cells for each metal composition with 10% molar excess of SnF_2 over SnI_2 and 5% $Pb(SCN)_2$ addition. Error corresponds to standard deviation and the champion metric is given in parentheses.

Sn Fraction (%)	PCE (%)		J_{sc} $\left(\frac{mA}{cm^2}\right)$		V_{oc} (V)		FF (%)		SPO (%)
	Forward	Reverse	Forward	Reverse	Forward	Reverse	Forward	Reverse	
30%	15.9 ± 0.8 (17.4)	16.0 ± 0.8 (17.6)	26.9 ± 1.2 (29.0)	26.5 ± 1.4 (28.7)	0.81 ± 0.03 (0.83)	0.82 ± 0.01 (0.83)	69.7 ± 1.9 (72.2)	70.6 ± 1.9 (73.5)	16.0 ± 0.7 (17.6)

Table S6. Summary of mean photovoltaic performance metrics for $(FA_{0.83}Cs_{0.17})(Pb_{0.5}Sn_{0.5})I_3$ solar cells for each metal composition with 20% molar excess of SnF_2 over SnI_2 and 6% $Pb(SCN)_2$ addition. Error corresponds to standard deviation and the champion metric is given in parentheses.

Sn Fraction (%)	PCE (%)		J_{sc} $\left(\frac{mA}{cm^2}\right)$		V_{oc} (V)		FF (%)		SPO (%)
	Forward	Reverse	Forward	Reverse	Forward	Reverse	Forward	Reverse	
50%	16.1 ± 0.6 (17.5)	16.5 ± 0.7 (18.1)	27.7 ± 0.9 (29.9)	28.0 ± 0.9 (30.3)	0.77 ± 0.03 (0.81)	0.77 ± 0.02 (0.82)	75.5 ± 0.9 (77.7)	76.1 ± 1.4 (78.4)	16.4 ± 0.5 (18.0)

1.30 eV External Quantum Efficiency
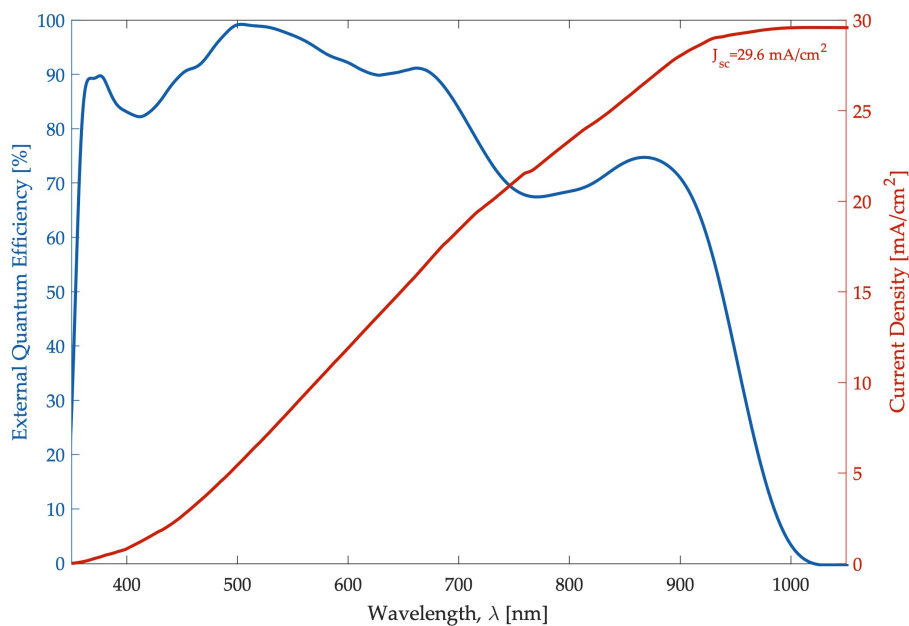
Figure S31 External quantum efficiency (EQE) spectra as measured by FTPS for the optimised $(FA_{0.83}Cs_{0.17})(Pb_{0.5}Sn_{0.5})I_3$ composition prepared on either ITO/PEDOT:PSS. The perovskite precursor contained a 6% molar excess of $Pb(SCN)_2$ with respect to PbI_2 and 20% molar excess of SnF_2 with respect to SnI_2.

1.33 eV Electroluminescence
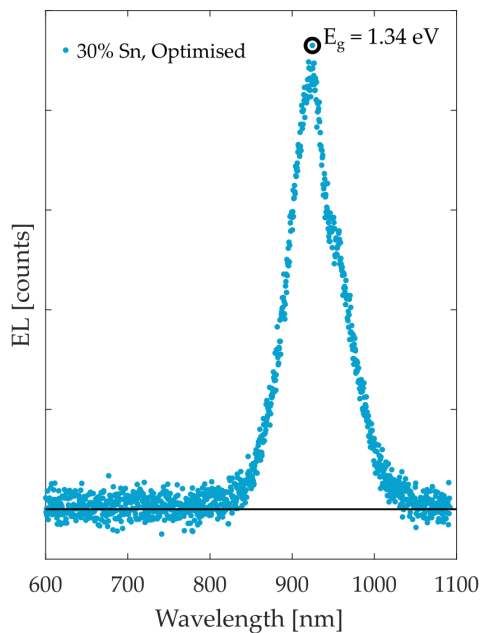
Figure S32. Electroluminescence spectra from optimised $(FA_{0.83}Cs_{0.17})(Pb_{0.7}Sn_{0.3})I_3$ solar cells.

References

1   C. L. Davies, J. B. Patel, C. Q. Xia, L. M. Herz and M. B. Johnston, *J. Infrared Millim. Terahertz Waves*, 2018, **39**, 1236–1248.

2   J. C. de Mello, H. F. Wittmann and R. H. Friend, *Adv. Mater.*, 1997, **9**, 230–232.

3   T. Seifert, S. Jaiswal, M. Sajadi, G. Jakob, S. Winnerl, M. Wolf, M. Kläui and T. Kampfrath, *Appl. Phys. Lett.*, 2017, **110**, 252402.

4   T. Seifert, S. Jaiswal, U. Martens, J. Hannegan, L. Braun, P. Maldonado, F. Freimuth, A. Kronenberg, J. Henrizi, I. Radu, E. Beaurepaire, Y. Mokrousov, P. M. Oppeneer, M. Jourdan, G. Jakob, D. Turchinovich, L. M. Hayden, M. Wolf, M. Münzenberg, M. Kläui and T. Kampfrath, *Nat. Photonics*, 2016, **10**, 483.

5   D. P. McMeekin, Z. Wang, W. Rehman, F. Pulvirenti, J. B. Patel, N. K. Noel, M. B. Johnston, S. R. Marder, L. M. Herz and H. J. Snaith, *Adv. Mater.*, 2017, **29**, 1607039.

6   D. P. Woodruff, *Modern Techniques of Surface Science*, Cambridge University Press, Cambridge, 3rd edn., 2016.

7   D. Briggs and M. P. Seah, *Practical Surface Analysis, Auger and X-ray Photoelectron Spectroscopy*, Wiley, 2nd edn., 1990woodruff.

8   H. J. Snaith, *Energy Environ. Sci.*, 2012, **5**, 6513–6520.

9   Y. Yu, C. Wang, C. R. Grice, N. Shrestha, J. Chen, D. Zhao, W. Liao, A. J. Cimaroli, P. J. Roland, R. J. Ellingson and Y. Yan, *ChemSusChem*, 2016, **9**, 3288–3297.

10 P. Terpstra and H. G. Westenbrink, *Proc. K. Ned. Acad. Van Wet.*, 1926, **29**, 431–442.

11 W. Ke, C. Xiao, C. Wang, B. Saparov, H.-S. Duan, D. Zhao, Z. Xiao, P. Schulz, S. P. Harvey, W. Liao, W. Meng, Y. Yu, A. J. Cimaroli, C.-S. Jiang, K. Zhu, M. Al-Jassim, G. Fang, D. B. Mitzi and Y. Yan, *Adv. Mater.*, 2016, **28**, 5214–5221.

12 H.-K. Nienhuys and V. Sundström, *Phys Rev B*, 2005, **71**, 235110.

13 R. Ulbricht, E. Hendry, J. Shan, T. F. Heinz and M. Bonn, *Rev Mod Phys*, 2011, **83**, 543–586.

14 R. A. Kaindl, D. Hägele, M. A. Carnahan and D. S. Chemla, *Phys Rev B*, 2009, **79**, 045320.

15 F. Urbach, *Phys Rev*, 1953, **92**, 1324–1324.